[American Journal of Science, Vol. 307, May, 2007, P. 793–832, DOI 10.2475/05.2007.02]

MAGNITUDE AND GEOMETRY OF REACTIVE FLUID FLOW FROM DIRECT INVERSION OF SPATIAL PATTERNS OF GEOCHEMICAL ALTERATION

BOSWELL A. WING* and JOHN M. FERRY**

ABSTRACT. Time-integrated equations governing tracer mass-balance provide a framework for interpreting spatial patterns of mineralogical, elemental, and isotopic alteration in rocks caused by reactive fluid flow, and linear inverse theory allows quantitative estimates of the magnitude and three-dimensional (3D) geometry of fluid flow. We demonstrate the inverse technique with a simple model system that involves fluid advection and fluid-rock oxygen isotope exchange only. Analytic forward models of reactive transport enable patterns of isotope alteration to be calculated exactly, and inversions of the resulting spatial patterns of synthetic isotope composition demonstrate the effectiveness of our approach.

For a field application of the inverse method, we consider regional metamorphic rocks from the Waits River Formation, southeastern Vermont, that expose a mineralogical and stable isotopic record of reactive fluid flow over an area of ≈120 km^2. Spatial patterns of prograde changes in whole-rock CO_2, $\delta^{18}O$, and $\delta^{13}C$ allow a direct inversion for the magnitude and 3D geometry of reactive flow at the time of final prograde mineral reaction. Consistency tests suggest that the inverse estimate is primarily controlled by patterns of CO_2 changes, and resolution tests indicate that the smallest features in the inverse flux field that can be reliably detected have an east-west dimension of ≈5 km and a north-south dimension of ≈14 km. The regionally-averaged time-integrated fluid flux vector returned by the inversion has a magnitude of 2.2×10^4 mol fluid/cm^2 rock, trends 255° in the horizontal plane, and is directed upward at 32° from the horizontal. The geometry of terrain-scale reactive flow was largely controlled by regional structure. Reactive fluids that entered the study area appear to have been tectonically-driven horizontally from the east at a depth ≈0.5 to 2.0 km beneath the present level of exposure.

INTRODUCTION

Reconstruction of the spatial patterns of ancient fluid flow in the field is a prerequisite for understanding the role of chemically reactive fluids in numerous geochemical and petrologic processes such as metamorphism, formation of many ore deposits, and global element cycles, particularly that for carbon (for example, Ague, 2004; Barnes, 1997; Kerrick and Caldeira, 1998; Kerrick, 2001). Even in the absence of chemical reaction between rock and fluid, patterns of ancient fluid flow are further relevant to physical and mechanical processes such as heat transfer in the crust and deformation in shear zones (for example, Fisher and Becker, 2000; Badertscher and others, 2002). The geological record of flow geometry in fossil fluid flow systems is the spatial pattern of mineralogical, isotopic, and geochemical alteration. Except in special occurrences (for example, Skelton and others, 1995), geochemical data have rarely been used to constrain the magnitude and three-dimensional (3D) geometry of reactive fluid flow on a regional scale. We present a general technique, based on inverse methods, for directly inverting mapped patterns of mineralogical, isotopic, and whole-rock chemical alteration to estimate the magnitude and 3D geometry of the associated reactive fluid flow.

*Department of Earth and Planetary Sciences, McGill University, Montreal, Quebec, Canada H3A 2A7; wing@eps.mcgill.ca

**Department of Earth and Planetary Sciences, Johns Hopkins University, Baltimore, Maryland 21218 USA

The amount of fluid that chemically interacted with rock can be rigorously measured as a fluid-rock ratio (Taylor, 1977) only for a flow system as a whole. Meaningful application of fluid-rock ratios therefore requires that the size of the system be identified and that appropriate average tracer abundances within the system be measured. These quantities, however, are not easily obtained in practice. Furthermore, fluid-rock ratios provide no information about the direction of ancient fluid flow. As a complement to a whole-system constraint provided by a fluid-rock ratio, tracer mass balances can provide additional quantitative constraints on the amount and direction of fluid flow at smaller scales (Bickle and McKenzie, 1987; Blattner and Lassey, 1989; Bickle and Baker, 1990; Baumgartner and Ferry, 1991; Lichtner, 1996; Ague, 2003). A local model that successfully reproduces a set of tracer measurements describes a possible mechanism, or combination of mechanisms, of fluid-rock interaction. However, different transport processes can lead to similar local patterns of tracer distributions (Baker and Spiegelman, 1995), and any set of real tracer measurements often can be interpreted in terms of a variety of reaction and transport processes that can be easily resolved only for mineralogically simple rocks (Abart and Sperb, 1997; Eppel and Abart, 1997; Abart and Pozzorini, 2000).

Our technique combines previous approaches both by solving for a time-integrated flux field that can have variable direction and magnitude at local scales and at the same time by satisfying an integrated whole-system tracer mass balance. It recognizes that the field pattern of mineralogical, isotopic, and geochemical alteration results from a combination of processes of mass transport and chemical reaction that may not or cannot be explicitly accounted for in the analysis. The analysis, nevertheless, indirectly, but quantitatively, considers the unaccounted processes by lumping their effects into a single misfit term. Our method is borrowed liberally from studies of atmospheric transport, physical oceanography, and Earth's magnetic field (for example, Bolin and Keeling, 1963; Wunsch, 1978; Gubbins, 1982). Inverse methods have been applied to other problems in geochemistry and petrology (for example, Allegre and Lewin, 1989; McKenzie and O'Nions, 1991; Albarede, 1995; Gaillardet and others, 1999) but, to our knowledge, never before to ones involving coupled fluid transport and chemical reaction.

METHODOLOGY

Model Equations

The primary time-integrated tracer mass balance equation we used is:

$$\mathbf{q} \cdot \nabla C_i - N_i + C_i N_f = e_i, \tag{1}$$

where $\mathbf{q}$ is the molar time-integrated fluid flux, C_i is the molar concentration of tracer species i in fluid, and N_i and N_f are the change in the molar amount of i and of total fluid, respectively, over the duration of flow and fluid-rock reaction (see Appendix A). The left-hand side of equation (1) expresses a pointwise balance between the tracer supplied to or removed from a reaction site by advection, $\mathbf{q} \cdot \nabla C_i$, and that taken up from or released to the fluid through mineral-fluid reaction, $(N_i - C_i N_f)$. Equation (1) therefore does not contain explicit consideration of mass transport by hydrodynamic dispersion, reaction kinetics, possible variations in fluid composition over the duration of flow and reaction, and changes in rock volume during or after reaction (Appendix A). A perfect balance among the terms on the left-hand side of equation (1) therefore is not expected. The effects of all the processes that are not explicitly accounted for are quantitatively represented by the single misfit term, e_i. For inversion of field data, equation (1) must be expressed in terms of specific molecular and isotopic tracers, areally integrated over the domain of the inversion, and discretized into a form suitable for numerical calculations.

Pointwise balance for molecular and isotopic tracers.—We applied the balance in equation (1) using one molecular tracer species (CO_2) and two isotopic tracer species ($\delta^{18}O$ and $\delta^{13}C$). Assuming the fluid is a binary H_2O-CO_2 solution ($X_{CO_2} + X_{H_2O} = 1$), the tracer abundance terms are expressed as

$$\begin{aligned} C_{CO_2} &= X_{CO_2}, \\ C_{\delta^{18}O} &= \delta^{18}O_f(2X_{CO_2} + X_{H_2O}) = \delta^{18}O_f(X_{CO_2} + 1), \\ C_{\delta^{13}C} &= \delta^{13}C_f(X_{CO_2}), \end{aligned} \tag{2}$$

where X_{CO_2} is the mole fraction of CO_2 in the fluid, and $\delta^{18}O_f$ and $\delta^{13}C_f$ the isotopic compositions of the fluid in standard δ notation (O, V-SMOW standard; C, V-PDB standard). The molar source terms in equation (1) are

$$\begin{aligned} N_{CO_2} &= -\underset{M}{\Delta}\rho_{CO_2,r}, \\ N_f &= -\underset{M}{\Delta}(\rho_{CO_2,r} + \rho_{H_2O,r}), \\ N_{\delta^{18}O} &= -\underset{M}{\Delta}\delta^{18}O_r(2\rho_{CO_2,r} + \rho_{H_2O,r}), \\ N_{\delta^{13}C} &= -\underset{M}{\Delta}\delta^{13}C_r(\rho_{CO_2,r}), \end{aligned} \tag{3}$$

where $\rho_{CO_2,r}$ and $\rho_{H_2O,r}$ are the molar density of CO_2 and H_2O in the rock, respectively, and $\delta^{18}O_r$ and $\delta^{13}C_r$ refer to the isotopic composition of the rock. Terms like $\underset{M}{\Delta}\rho_{CO_2,r}$ are the total change in $\rho_{CO_2,r}$ in a rock over the duration of an alteration event as measured in an appropriate geochemical reference frame (see Appendix A). Equations (2) and (3) assume rock porosity during the infiltration event was finite but negligible in terms of tracer storage.

Conservation of isotopic tracers is expressed in delta notation and is based on two reasonable assumptions. First, oxygen and carbon isotopes in the fluid-rock system are assumed to be dominated by the light isotopes, ^{16}O and ^{12}C, that allows molar isotopic concentrations to be well-approximated by isotope ratios. Second, total fluid conservation is assumed because differences in isotope ratios relative to a standard ratio (that is, δ values) are conserved rather than the isotope ratios themselves.

Areal integration of the tracer mass balance.——The tracer mass balance in equation (1) applies pointwise over a representative elemental volume (REV) of rock that is large compared to textural and compositional variations in hand specimen or thin section but small compared to regional variations in C_i, N_i, or N_f. Most geological studies involve a two dimensional distribution of samples on a scale much larger than a REV, and integration of equation (1) over the study area, A_d, places a simple mass balance check on the time-integrated flux through the rocks that separate different samples. This integration,

$$\int_{A_d} \mathbf{q} \cdot \nabla C_i dA = \int_{A_d} (N_i - C_i N_f) dA + \int_{A_d} e_i dA = \int_{A_d} N_i^* dA + \int_{A_d} e_i dA, \tag{4}$$

expands the local balance between tracer supply or removal and tracer production or consumption to a regional scale. The N_i^* notation in equation (4) expresses the difference between the total tracer change in a rock, N_i, and the change that accompanies the net loss or gain of fluid, $C_i N_f$, and it provides a measure of the degree

to which a rock behaved as a closed system during alteration. If the study area was a closed system in the petrologic sense, then the integral of N_i^* over the region defined by A_d will be zero; a non-zero negative N_i^* implies supply of tracer from external sources, while a non-zero positive N_i^* implies tracer removal to external sinks.

Approximation of the integral mass balance.—The integral balance in equation (4) is the basis for the inverse method, and we approximated its solution through the finite element method. Early inverse studies of ocean circulation expressed similar integral mass balances through a control volume approach (Wunsch, 1978) or a finite difference approach (Fiadeiro and Veronis, 1984). The finite element approximation was used for three reasons. First, the method allows for a compact consideration of errors from an imperfect knowledge of both process and distribution of data. Second, the approximation of the concentration and source term fields and the discretization of the mass balance equations are accomplished simultaneously. Third, geological samples are often collected non-uniformly in space in order to capture changes in alteration style or intensity. The primary advantage of the finite element method is that it has the flexibility to represent an arbitrary sample distribution connected by an irregular grid of variably-sized elements. We used a Delaunay triangulation to construct a finite-element grid. The Delaunay triangulation divides the sample domain into regions defined by triplets of sample locations that are closer to each other than any other points (Baker, 1999). It can be constructed for any arbitrary distribution of points, and it is unique in two dimensions unless the same circle circumscribes four or more sample points (Braun and Sambridge, 1995).

In the finite-element method, continuous functions in the governing continuum equations (for example, $\mathbf{q}$, C_i, and N_i^*) are replaced by discrete values that are defined at the grid nodes and trial functions that describe how the values vary from node to node (Zienkiewicz and Morgan, 1983). Substitution of these trial function approximations into equation (4) will not satisfy the mass balance generally and leaves a domain residual, d_i. Mass balance can be enforced through an integral of the weighted total residual over the entire sample domain (Finlayson, 1972). If $\mathbf{q}$, C_i, N_i^*, d_i, and e_i are replaced by their trial function approximations (denoted by a tilde) and weighted over A_d, equation (4) takes the following form,

$$\int_{A_d} G_l(\tilde{\mathbf{q}} \cdot \nabla \tilde{C}_i - \tilde{N}_i^*)dA = \int_{A_d} G_l(\tilde{e}_i + \tilde{d}_i)dA = \int_{A_d} G_l(\tilde{u}_i)dA \quad l = 1. . .m, \tag{5}$$

where G_l represents a global trial function, $\tilde{u}_i$ is a trial function approximation of the allowable total residual u_i, and m is the total number of grid nodes (that is, sample locations) in the domain. Equation (5) shows that two sources of error will control the uncertainty of the inverse method. The first, represented by e_i, is due to neglected processes, and the second, represented by d_i, is the domain residual due to approximation. While contributions from each error source determine how much of a total misfit in tracer conservation should be tolerated, their individual effects are difficult to separate in practice.

The discrete form of equation (5) depends in detail on the functional form chosen for the approximations, $\tilde{\mathbf{q}}$, $\tilde{C}_i$, and $\tilde{N}_i^*$, and the weighting functions, G_l. In the Galerkin finite-element method, residuals are weighted by the same trial functions used to make the approximations (Finlayson, 1972). We used linear trial functions and followed standard procedures for constructing Galerkin systems (Zienkiewicz and Morgan, 1983), which results in the following discrete equivalent to equation (5),

$$\underline{\underline{\mathbf{G}}}\,\underline{\mathbf{q}} = \underline{\mathbf{n}} + \underline{\mathbf{u}} \tag{6}$$

Here, $\underline{\underline{\mathbf{G}}}$ is a concatenation of the finite-element stiffness matrices that describe the gradients and grid geometry that control conservation of each of the tracers, $\underline{\mathbf{q}}$ is a vector that contains the three components of the flux at each grid point, $\underline{\mathbf{n}}$ is a load vector that expresses the weighted source terms for each of the tracers, and $\underline{\mathbf{u}}$ is a misfit vector that encompasses the lack of conservation for each of the tracers and the fluid. Both $\underline{\underline{\mathbf{G}}}$ and $\underline{\mathbf{n}}$ are defined by measured data and the geometry of the sample distribution. The presence of the misfit vector in equation (6) suggests that a particular solution for $\underline{\mathbf{q}}$ will depend on the acceptable range of values for $\underline{\mathbf{u}}$. We used the geometrical characteristics of the Delaunay triangulation and a simple Monte Carlo resampling procedure to estimate acceptable uncertainty in equation (6), although the recognition of process and approximation as separate error sources may lead to a more sophisticated estimation scheme in the future.

Error Analysis

The inverse method includes an explicit recognition that the equations we used are an incomplete description of all details of mass transport and mineral-fluid reaction during metamorphism and that their representation of these processes is only approximate. Our error estimation procedure assumes that neighboring samples exhibit similar geochemical characteristics more often than not. Source term variability in neighboring rocks, therefore, became a surrogate for the acceptable mass balance misfit in a given region. We assigned misfit based on the spatial resolution and local connectivity of the measured source term data.

Estimation of mean sources and their uncertainty.—The Delaunay triangulation allows for the region of influence around each node to be quantitatively estimated (for example, Carlson, 1991). Each location was assigned a list that includes the point itself and all other points to which it is connected. These points are the closest locations from which measured data are available, and they form the natural neighbors of the original sample point (Watson, 1992). We considered that the measured source terms associated with the samples on this list provide a permissible range of values for the original measurement at the sample point.

In the Monte Carlo step of the error estimation procedure, the source term at each point was replaced by a value chosen randomly from the list of source terms associated with that point and its natural neighbors. The resampling scheme is a slight variant of the bootstrap method because we generated data replicates from the point and its natural neighbors rather than from the entire data set (compare Ague, 1994; Ague and van Haren, 1996). Once this was completed for all sample points within the region of interest, an areal average source term for j-th Monte Carlo trial was calculated as

$$\bar{N}^{*}_{i,j} = \frac{1}{A_m} \int_{A_m} \tilde{N}^{*}_{i,j} dA, \quad j = 1. \; . \; .n, \tag{7}$$

where A_m represents the area over which the average is estimated, the overbar indicates an average value, and the tilde denotes that the variation between grid points is approximate. The calculation was repeated for $n \approx 10^4$ trials, and the collection of resulting values provided an empirical distribution function for the source term over A_m (Efron and Tibshirani, 1993). We estimated the bootstrap mean and standard error of $\bar{N}^{*}_{i}$ for each tracer averaged over the entire domain of the inversion (that is, we took $A_m = A_d$) from the mean and standard deviation of the empirical distribution function (Efron and Tibshirani, 1993). These source term statistics were the basis for estimating the acceptable misfit in the inverse procedure.

For each tracer, we first divided the standard deviation of the empirical distribution function by the bootstrapped mean areal source term. This quantity was multiplied by the ratio of probabilities for the bootstrapped mean areal source term and the measured mean areal source term, calculated according to the empirical distribution function. The resulting tracer correction factor was an attempt to account for bias introduced by the resampling procedure. At each node, we then compared the bootstrap error for each tracer with the product of the correction factor for tracer i and the measured N_i^* value, and took the larger of the two as the acceptable misfit, $\sigma_{N_{ij}^*}$, for tracer i at sample location j. The relative covariance, $\underline{\underline{\mathbf{C}}}^{-1}$, of the effective tracer source terms was computed from the ratio of $\sigma_{N_i^*}$ to N_i^* at each location.

Model Solution

The solution of a linear inverse problem typically relies on two competing requirements: the inverse solution should fit measured data within prescribed error limits, and it should exhibit only the structure demanded by the data. We used a standard technique of solution regularization known as damped (Menke, 1989) or weighted tapered least-squares (Wunsch, 1996). The solution is obtained by considering its smoothness in concert with its associated residual error. Once a smoothness measure is defined, solutions of a linear inverse problem fall on a trade-off curve between smoother solutions with larger residual error and rougher solutions with smaller residual error. A rougher solution may end up fitting the data more precisely, but the detailed structure in a rougher solution is inherently less reliable than the broad structure in a smoother solution (Parker, 1977).

Our inverse method extracts the smoothest time-integrated fluid flux field that satisfies mass balance constraints within their estimated error by minimizing the following quantity:

$$F = \underline{\mathbf{u}}^T \underline{\underline{\mathbf{W}}}\, \underline{\mathbf{u}} + \lambda^2 \underline{\mathbf{q}}^T \underline{\underline{\mathbf{S}}}\, \underline{\mathbf{q}} \tag{8}$$

The misfit contribution to F is weighted in the least-squares sense by a matrix, $\underline{\underline{\mathbf{W}}}$, that governs how much importance should be attached to a given mass balance equation. Likewise, the flux field contributes misfit to F through the influence of a matrix, $\underline{\underline{\mathbf{S}}}$, that regulates variability in the flux field's structure. The trade-off parameter, λ, controls the relative importance of these two terms and, ultimately, determines the final inverse solution (Parker, 1977; Wunsch, 1996).

Weighting and regularizing the inverse solution.—We took $\underline{\underline{\mathbf{W}}}$ to be the inverse of the expected relative covariance, $\underline{\underline{\mathbf{C}}}^{-1}$, of the effective tracer source terms. We assumed mass-balance misfits for different tracers were uncorrelated, which led to a diagonal covariance matrix. (In the field application presented later, the resampling procedure revealed negligible correlation between CO_2 and $\delta^{18}O$ and between CO_2 and $\delta^{13}C$, and only minor correlation between $\delta^{18}O$ and $\delta^{13}C$.) Non-zero off-diagonal terms could be incorporated into the covariance matrix if the data or the problem warranted it. Prior to weighting by $\underline{\underline{\mathbf{W}}}$, each row in $\underline{\underline{\mathbf{G}}}$ was divided by its norm to minimize the influence of the measurement units for each tracer (Wunsch, 1996).

The smoothness matrix, $\underline{\underline{\mathbf{S}}}$, was constructed so that the matrix product, $\underline{\underline{\mathbf{S}}}_{\mathbf{q}}$, represented the discrete version of the quantity, $\int_{A_d} \nabla_h^2 \mathbf{q} dA$, where the h subscript indicates the Laplacian operator over the two dimensions that define the inverse region (compare Provost and Salmon, 1986; Bloxham and Jackson, 1992; Rau and others, 2000). Its practical significance is that it dampens flux variations among adjacent nodes to prevent the solution from overfitting the data. We applied the constraint in its weak finite-element form (Zienkiewicz and Morgan, 1983), which leads to a natural boundary condition that requires continuity in the time-integrated flux field across the boundaries of each element.

Choice of an inverse solution.—An inverse solution is completely defined by the trade-off parameter, λ, once a weight matrix and a smoothness matrix have been chosen. In effect, the number of free parameters in the problem is reduced from 3M (q_x, q_y, q_z at each of the M sample locations) to one. We chose λ such that our solution just fits the data according to a reduced chi-squared measure (Constable and others, 1987):

$$\chi^2_\nu \equiv \frac{1}{\nu} \sum_{j=1}^{\nu} \left(\frac{\sum_k G_{jk} q_k - n_j}{\sigma_{N^*_j}} \right)^2 = 1, \tag{9}$$

where χ^2_ν is the reduced chi-squared statistic, ν is the number of data that constrain the inverse solution, G_{jk}, q_k, and n_j represent term-wise equivalents to $\underline{\underline{\mathbf{G}}}$, $\underline{\mathbf{q}}$, and $\underline{\mathbf{n}}$, and $\sigma_{N^*_{i,j}}$ is the acceptable misfit for tracer $\bar{N}^*_i$ at sample location j. The model solution that returns a reduced chi-squared value of one is the optimal solution for data with independent, normally distributed errors (Bevington and Robinson, 1992). It provides a reproducible framework for evaluating and comparing inverse solutions in the case where error distributions are unknown or complex (Constable and others, 1987; Parker, 1994). Other methods of selecting a trade-off parameter (the L-curve; van Wijk and others, 2002) or an inverse solution (the truncated SVD; Brown, 1995) gave final models that differed in detail but not substance from results presented here.

DEMONSTRATION OF THE INVERSE METHOD

An imbalance exists in the final expression for regional tracer mass balance because of neglected local processes and finite sample coverage. Both misfit sources contribute to the uncertainty of an inversion based on field data and, consequently, demonstration of the inverse method independent of uncertainty in local process is impossible in applications to field data. We therefore calculated synthetic data from a simple forward model of fluid-rock interaction in which the pointwise balance between tracer transport and reaction held exactly. The finite element approximation then is the only source of misfit in inversions of the synthetic data. We compared the flux fields from synthetic inversions with the imposed ("true") fluxes from the forward model to demonstrate the inverse method and to investigate the error inherent in it.

Characteristics and Results of the Forward Model

We based our forward model on the simplified dynamics that govern steady thermal convection in a long, thin, two-dimensional segment of crust (see Appendix B). The advantage of this geometrical simplification is that the flow field can be represented exactly by an analytical formulation (Phillips, 1991), and the isotopic alteration produced by fluid flow can be calculated directly. Although we chose specific numerical parameters for our model relevant to fluid flow in oceanic crust (see Appendix B), empirical permeability relationships (Manning and Ingebritson, 1999) imply that results for a depth-rescaled model would be relevant to continental crust as well (for example, fluid flow during regional metamorphism). The forward calculations considered oxygen isotopic alteration caused by fluid flowing along a temperature gradient with local mineral-fluid equilibrium (Dipple and Ferry, 1992). The calculated results provided C_i and N^*_i values for $i = \delta^{18}O$ that were used as input to the synthetic inversions.

Details of heat and fluid flow in the model and calculation of oxygen isotope alteration are given in Appendix B. Fluid transport in the forward model was driven by, but did not alter, the specified conductive temperature distribution (fig. 1). The model temperature distribution is illustrated in figure 1A; horizontal gradients average ≈0.05°C/km with a maximum of ≈2°C/km. These gradients lead to horizontal density

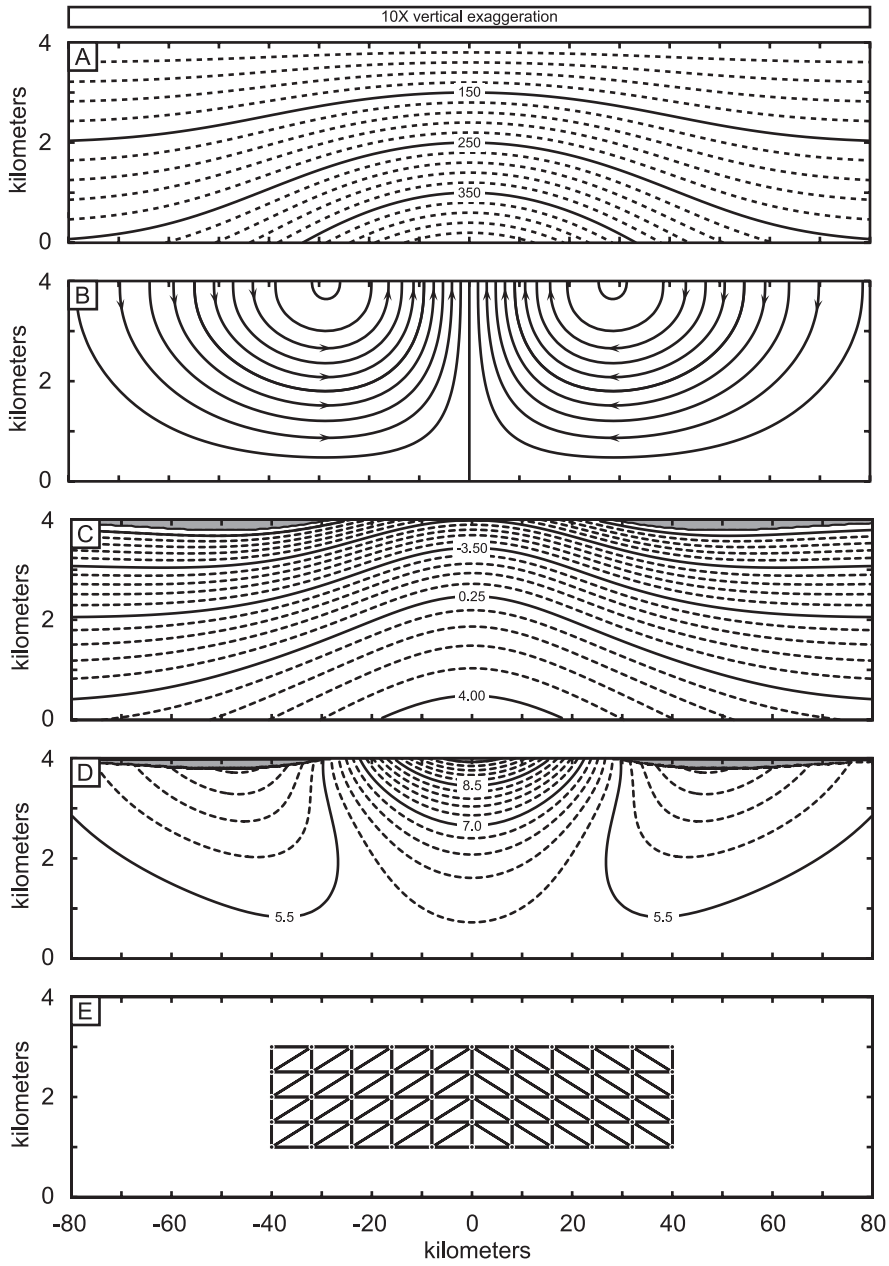

Fig. 1. Elements of the forward model used to generate synthetic data for validity tests. (A) Steady-state temperature distribution over the model domain. Upper boundary is 50°C. Geothermal gradient at the lower boundary decreases exponentially away from the center of the domain with a characteristic width of 40 km and ranges from a peak value of 100°C/km at the center of the domain to a background value of 50°C/km at the edges. (B) Steady state flow field resulting from the temperature distribution in figure 1A. Flow field is contoured with the molar stream function, Ψ_m. Contour spacing is 1.3×10^8 mol fluid/cm/Ma. (C) Oxygen isotope distribution in the fluid after 5 Ma of flow illustrated in figure 1B through the temperature distribution in figure 1A. Initial $\delta^{18}O$ of the pore fluid is set by equilibrium with the rock. Infiltrating fluid has $\delta^{18}O = 0‰$ (V-SMOW). Gray shading indicates region where pore fluid has $\delta^{18}O = 0‰$. (D) Oxygen isotope composition of rock after 5 Ma of flow in figure 1B through temperature distribution in figure 1A. Initial $\delta^{18}O$ of the rock is 5.5‰ (V-SMOW) and fluid-rock fractionation is calculated from experimental data (Cole and others, 1987). Gray shading indicates region where rock is in equilibrium with a pore fluid that has $\delta^{18}O = 0‰$. Rock $\delta^{18}O$ is >10‰ in this region. (E) Spatial relationship between the inversion domain and the domain of the forward model. A representative inverse grid of 11 nodes in the horizontal direction and 5 nodes in the vertical direction is illustrated.

variations that cause fluid motion. The resulting flow field is illustrated in figure 1B. The spacing between the contours in figure 1B corresponds to representative Darcy velocities of ≈1 mm/yr. The oxygen isotope compositions of the model fluid and rock were calculated assuming local fluid-rock equilibrium. Final model fluid and rock $\delta^{18}O$ values are controlled by the duration of fluid flow. The spatial distribution of $\delta^{18}O$ of model fluid and rock after 5 Ma of infiltration is presented in figures 1C and 1D, respectively. We used a subset of the results calculated for 5 Ma of alteration in the inversion demonstration.

Inversion of Synthetic Data

We inverted calculated fluid and rock $\delta^{18}O$ values from a region (80 km by 2 km) at the center of the model domain to minimize boundary effects (fig. 1E). Inversions proceeded in three steps: (1) calculated rock and fluid $\delta^{18}O$ datasets were sampled onto inverse grids of varying resolution; (2) an appropriate level of misfit for the inversion was determined from the Monte Carlo statistics of the gridded data; and (3) the gridded data were inverted for a time-integrated flux field that produces a comparable misfit according to equation (9). We validated the synthetic inversions by calculating the correlation between the imposed "true" time-integrated flux ($\mathbf{q}$) and the estimated inverse flux ($\mathbf{q}'$),

$$\text{Correlation} = \frac{\int_{A_d} \mathbf{q} \cdot \mathbf{q}' dA}{\sqrt{\int_{A_d} \mathbf{q}' \cdot \mathbf{q}' dA \int_{A_d} \mathbf{q} \cdot \mathbf{q} dA}} \tag{10}$$

The correlation measures the average parallelism between the two fluxes, and ranges from +1 (perfectly parallel) to -1 (perfectly anti-parallel).

A representative inversion is presented in figure 2, based on an 11 by 5 inverse grid (fig. 1E), and the $\delta^{18}O$ distributions after 5 Ma of fluid flow (figs. 1C, 1D). The "true" time-integrated flux field in figure 2A was calculated by integrating the molar flux in figure 1B with respect to time at each node in the grid. Figure 2B illustrates the inverse time-integrated fluxes. The two fields are nearly identical, with the inverse flux field slightly more uniform. The inverse solution correlates with the "true" fluxes in figure 2A at >99 percent according to equation (10).

The inverse solution in figure 2B produced a misfit in the $\delta^{18}O$ distribution in the rock (fig. 2C). This misfit distribution produces a reduced chi-squared value of exactly one relative to the misfit allowed by the synthetic source terms on the 11 by 5 grid. Monte Carlo resampling of the gridded $N^*_{\delta^{18}O}$ values gave a bootstrap estimate of the areal average $N^*_{\delta^{18}O} = -0.15$ permil and a standard error of 0.05 permil; the associated relative misfit was 30 percent. We used these values and the synthetic data to define the covariance, $\underline{\underline{\mathbf{C}}}^{-1}$, of the synthetic source terms and their acceptable misfit, $\sigma_{N^*_{\delta^{18}O}}$. Most of the misfit is concentrated in the upflow region in the center of the inverse domain where the magnitude of alteration is greatest. There is an effectively constant relative misfit over the entire domain.

Misfit in the tracer mass balance leads to uncertainty in the inverse flux field. We calculated this uncertainty for the representative synthetic inversion by standard error propagation techniques (Menke, 1989; Wunsch, 1996). The uncertainty in the inverse solution is shown in figure 2D at the 2σ level, along with the vector differences between the flux fields in figures 2A and 2B. Most of the flux differences lie within the 2σ ellipses, as expected from the degree of correlation between the "true" and inverse

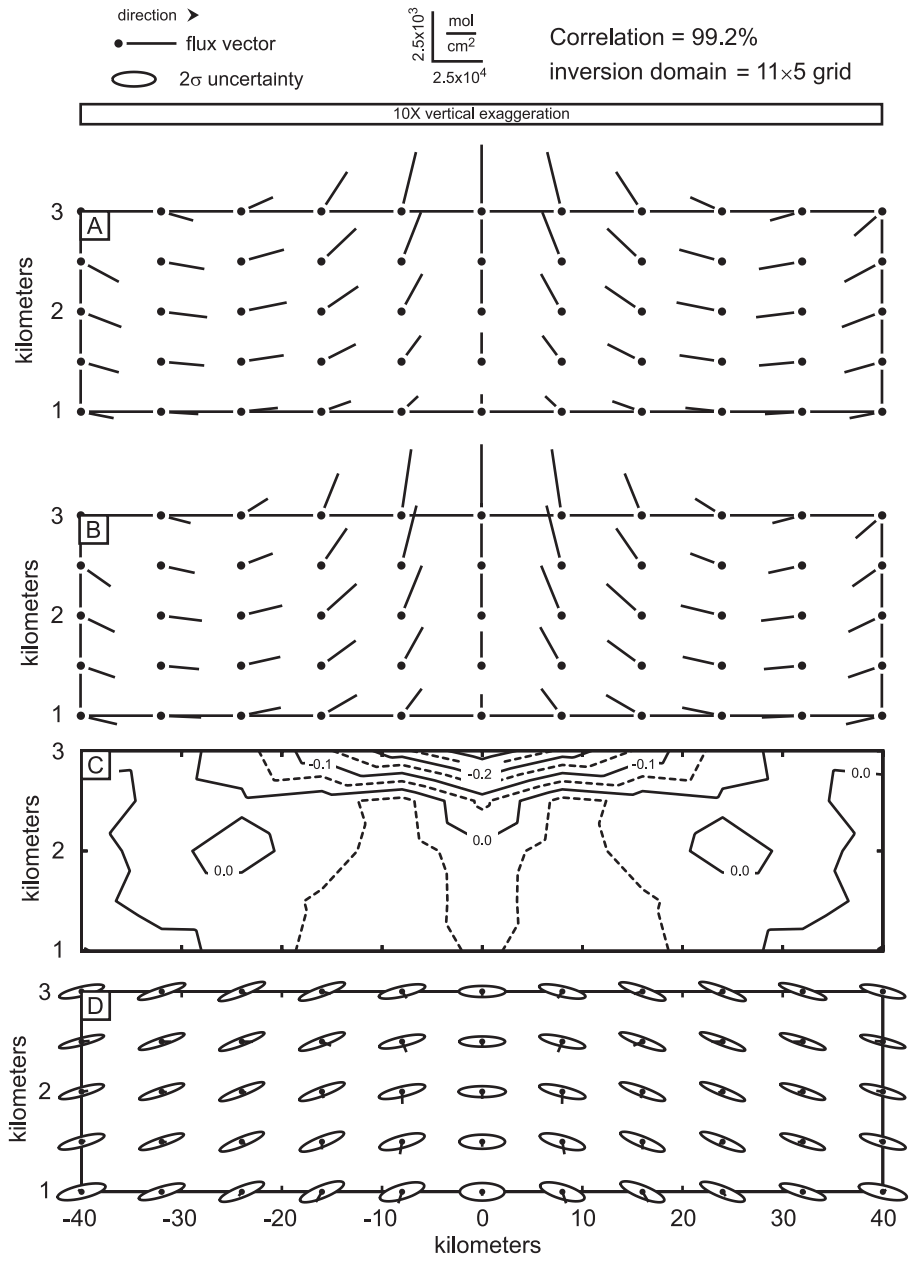

Fig. 2. Representative inversion of synthetic data on an 11 by 5 grid. (A) Input time-integrated flux field at each point on the grid. Flux field represents the integration over 5 Ma of the imposed, "true" fluxes shown in figure 1B. (B) Inverse calculation of time-integrated flux field at each point in the grid. Flux field is calculated from the $\delta^{18}O$ values shown in figures 1C and 1D sampled at every node in the grid. Inverse flux field correlates with the imposed flux field at a >99% level. (C) Misfit between the $\delta^{18}O$ rock values in the synthetic data set and those predicted by the inverse model (in ‰). Misfit values are largest where the total $\delta^{18}O$ shift in the rock is greatest. (D) Difference between the input and inverse flux at each grid point, along with uncertainty estimates from the inverse flux model. Differences are almost all within the 2σ uncertainty limits predicted from the model.

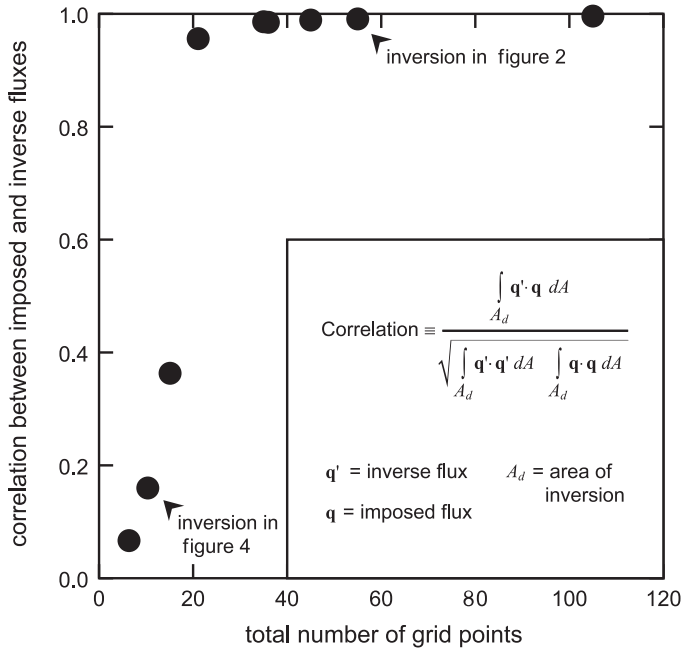

Fig. 3. Correlation between the imposed "true" and calculated inverse flux fields as a function of the total number of grid points in the inverse domain. Arrowheads identify representative inversions from figures 2 and 4. Technique accurately predicts the imposed fluxes down to an element area of ~10 km^2. Sharp drop-off in correlation at 20 grid points is characteristic of the relationship between the accuracy of an inversion and its resolution.

fluxes. The orientation of the 2σ ellipses indicates that most of the inverse flux vectors exhibit a significant degree of covariation between their vertical and horizontal components. This covariation is not present in $\underline{\underline{\mathbf{C}}}^{-1}$ (which is diagonal) and arises solely because of the grid geometry and finite-element representation used in the inverse method.

We investigated the performance of the inverse method as a function of the resolution of the inverse grid. The correlation between the "true" and inverse fluxes exhibits a step function-like dependence on the number of inverse grid nodes (fig. 3). For grids with ≥21 nodes, the inverse and true flux fields are correlated at a level >95 percent. The correlation drops off sharply for inversions performed on grids with <21 nodes. On average, only ≈10 percent of the deviation from perfect correlation is produced by an inability to resolve flux variability among grid points. The dominant contribution to the drop-off in correlation develops from differences between the inverse and "true" flux fields at each node. Larger differences between inverse and "true" flux fields at each grid node result directly from increased smoothing of the solution as the number of grid nodes decreases. The smoothness constraint has a greater influence on the coarse grid inversions because coarser grids allow greater relative misfit than finer grids. In concert with decreasing correlation, inversions based on coarsely resolved data predict greater uncertainties in the final flux estimate. Therefore, even when inverse fluxes correlate poorly with the "true" fluxes, they are often statistically indistinguishable.

A representative inversion using <21 nodes (5 by 2 grid) is illustrated in figure 4. The $N^*_{\delta^{18}O}$ values were resampled on this grid for an estimated areal average

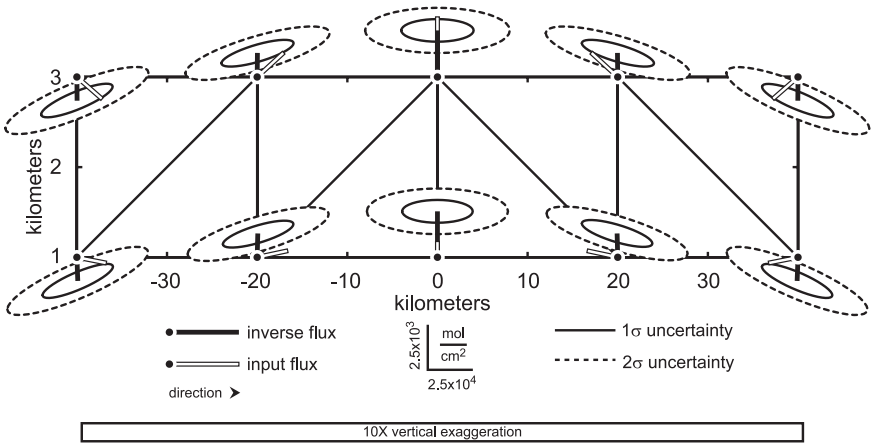

Fig. 4. Representative inversion of synthetic data on a 5 by 2 grid. Thick black lines represent calculated fluxes, and thick white-filled lines show input fluxes on the same grid. Uncertainty estimates from the inverse procedure are shown as thin continuous (1σ) and dashed (2σ) ellipses at each point. Diagonal lines in background define the 5 by 2 grid on which the inversion was performed. The sharp drop-off in correlation in figure 3 results primarily from the inability of the coarse grid to capture inter-element flux variability.

$N^{*}_{\delta^{18}O} = -0.31$ permil and a standard error of 0.18 permil. A relative misfit of 60 percent was applied to the synthetic data to calculate $\underline{\underline{\mathbf{C}}}^{-1}$ and the acceptable misfit. At a majority of the nodes, the difference between the "true" and inverse fluxes is within the predicted 2σ uncertainty limits. However, the inverse flux estimates are also within uncertainty of zero at most of the nodes. By estimating the uncertainties in the inverse solution, the method can identify cases where misfit estimates are so large that the inverse model returns essentially no useful information.

FIELD EXAMPLE OF MULTIPLE TRACER INVERSION

We performed an inversion, using CO_2, $\delta^{18}O$, and $\delta^{13}C$ as tracers, for a Barrovian regional metamorphic terrain in southeastern Vermont as an example of inverting field data. The exercise illustrates many of the issues faced by practical applications of the inverse methods, including irregular sample distribution, source term variability, combined inversion of molecular and isotopic tracer data, and resolution of features in the flux field.

Geological Setting

The inversion used data for the Waits River Formation (fig. 5), a turbidite composed of approximately equal amounts of metacarbonate rock and pelitic schist interbedded at a scale of 10 to 100 cm (Hepburn and others, 1984; Hatch, 1988). The Waits River Formation, along with the overlying Gile Mountain Formation, form a Siluro-Devonian metasedimentary belt that runs along the length of eastern Vermont (Doll and others, 1961; Hueber and others, 1990). The rocks of eastern Vermont were deformed and metamorphosed during the Devonian Acadian orogeny (Thompson and Norton, 1968; Thompson and others, 1968; Osberg and others, 1989). Deformation involved an earlier stage of west verging nappes and a later stage of broad domes (Rosenfeld, 1968; Thompson and others, 1968; Osberg and others, 1989). Regional isograds correspond to the appearance of biotite (Bt), garnet, and kyanite ± staurolite (Ky ± St) in pelitic schists and of oligoclase (Olig), Bt, amphibole (Amph), and diopside (Di) in metacarbonates (Doll and others, 1961; Hepburn and others, 1984; Ferry, 1992). The peak of metamorphism followed nappe formation and was

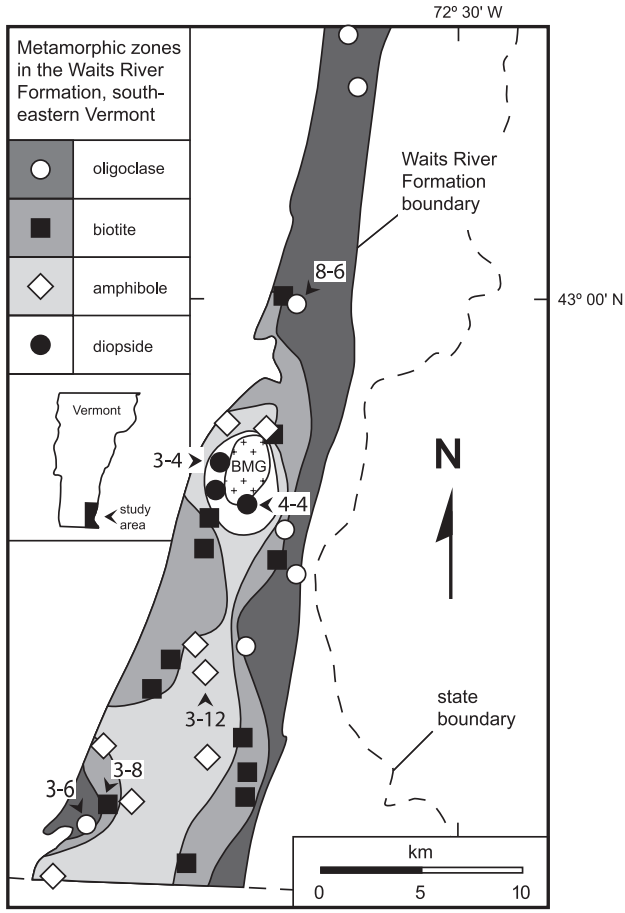

Fig. 5. Metamorphic map of carbonate rocks of the Waits River Formation in southeastern Vermont (after Ferry, 1992). BMG is the Black Mountain granite. Symbols represent sample locations that are the basis for the finite-element grid used in field inverse model. Sample numbers refer to representative samples from Ferry (1992).

concurrent with or occurred at the end of dome-stage deformation (Hepburn and others, 1984; Barnett and Chamberlain, 1991; Menard and Spear, 1994). Monazite Th-Pb ages from pelitic schists of the Gile Mountain Formation date the formation of Ky during Barrovian metamorphism at 353 ± 9 Ma (Wing and others, 2003).

The study focused on metacarbonate rocks of the Waits River Formation exposed in the Guilford structural dome and nearby regions (fig. 5; Hepburn and others, 1984). Amphibole-zone metacarbonate rocks form a broad metamorphic high coincident with the axis of the dome; Bt- and Olig-zone rocks occur outboard of the axis of the dome, and Di-zone rocks are confined to a km-scale aureole around the Black Mountain granite. The Ky + St isograd wraps around and is deflected by but not crosscut by the pluton (Hepburn and others, 1984), indicating emplacement of the granite was synchronous with Barrovian regional metamorphism. Based on structural and textural data for the granite and surrounding metamorphic rocks, Hepburn and others (1984) concluded that the contact aureole represents a "hot-spot" that developed "synchronously with the peak of metamorphism" or nearly so. Mineral equilibria

record P = 8 ± 1 kbar and T ≈500°C in the Olig zone, ≈530°C in the Bt zone, ≈545°C in the Amph zone, and ≈575°C in the Di zone (Ferry, 1992, 1994). Mineral equilibria additionally record that H_2O-CO_2 metamorphic fluids in the metacarbonate rocks were H_2O-rich with X_{CO_2} = 0.02-0.26 (Ferry, 1992). Decarbonation reactions, on the other hand, produced fluids with $CO_2/(CO_2 + H_2O) > 0.50$ (Ferry, 1992). This difference is a characteristic signature of infiltration-driven metamorphic decarbonation reactions (Rice and Ferry, 1982).

Complete data for mineral assemblages, modes, mineral compositions, whole-rock major-element compositions, and inferred prograde reactions are listed by Ferry (1992) for six representative samples of metacarbonate rock used in the inversion. These include samples 3-6 and 8-6 from the Olig zone, sample 3-8 from the Bt zone, sample 3-12 from the Amph zone, and samples 3-4 and 4-4 from the Diop zone (fig. 5).

Assumptions, Simplification, and Limitations

Distribution and number of samples.—Because the inversion is based on data for samples collected for other purposes in an earlier study (Ferry, 1992), the distribution and number of samples is adequate but not ideal. The relatively low density and lack of uniformity of the sample distribution may not have captured all important aspects of metamorphic fluid flow in the area of figure 5. In particular, the sample distribution fails to represent the entire contact aureole that extends completely around the intrusion (Hepburn and others, 1984). Eight fictive sample locations therefore were added to the Di zone around the Black Mountain granite to adequately represent the contact aureole and to capture flux variations anticipated near the pluton-metasediment contact.

In addition, the inversion is based on data for only one sample collected from each location. The validity of assuming that one sample is representative of all metacarbonate rock at an outcrop can be assessed from a recent investigation of 48 samples from a single large exposure of metacarbonate rock in the Bt zone of the Waits River Formation elsewhere in eastern Vermont (Penniston-Dorland and Ferry, 2006). The standard deviations of X_{CO_2}, $\delta^{18}O_{calcite}$, and $\delta^{13}C_{calcite}$ (the latter two are proxies for $\delta^{18}O_f$ and $\delta^{13}C_f$) are 0.02, 0.3 permil, and 0.4 permil, respectively. The standard deviations are much smaller than the range in X_{CO_2}, $\delta^{18}O_f$, and $\delta^{13}C_f$ over the area of figure 5, 0.25, 7.1 permil, and 8.2 permil, respectively (Table 1 of Wing and Ferry, 2002). A single sample therefore is probably adequate for estimating C_i of each tracer at each location. Values of $N^*_{\delta^{18}O}$ and $N^*_{\delta^{13}C}$ correlate closely with $\delta^{18}O$ and $\delta^{13}C$ of carbonate, $\delta^{18}O_{carbonate}$ and $\delta^{13}C_{carbonate}$ (explained in a later section). Because standard deviations of measured values of $\delta^{18}O_{carbonate}$ and $\delta^{13}C_{carbonate}$ at the location investigated by Penniston-Dorland and Ferry (2006) are also small (0.3 and 0.4‰, respectively) relative to the range in measured $\delta^{18}O_{carbonate}$ and $\delta^{13}C_{carbonate}$ over the entire study area (9.8‰ and 8.4‰, respectively), data from single samples probably also provide adequate estimates of $N^*_{\delta^{18}O}$ and $N^*_{\delta^{13}C}$ at each location in the area of figure 5. Reaction progress, however, varies considerably among the 48 samples investigated by Penniston-Dorland and Ferry (2006). Although the standard deviation of $N^*_{CO_2}$ is correspondingly large, 0.67×10^{-3} mol CO_2/cm^3 rock, it is less than the range in $N^*_{CO_2}$ over the area in figure 5, $(0.00\text{-}3.57)\times10^{-3}$ mol CO_2/cm^3 (Wing and Ferry, 2002). Average values of $N^*_{CO_2}$ at each location are not as well constrained by data for single samples as are values of $N^*_{\delta^{18}O}$ and $N^*_{\delta^{13}C}$.

Progressive metamorphism and the timing of mineral-fluid reaction.—The inversion considers a duration of fluid flow at the time of final mineral reaction defined as the period between when the present minerals developed in a sample and when minerals characteristic of the immediately lower grade zone of metamorphism developed. The procedure therefore makes two assumptions. The first is that metamorphism was progressive over the time period considered. The assumption is reasonable because

mineral reactants of the devolatilization reactions that define the isograds in metacarbonate rocks often occur in samples collected near but on the high-grade side of the isograd. These reactants are always observed in samples near but on the low-grade side of the isograd. The second assumption is that the period of final mineral-fluid reaction considered by the inversion, measured in absolute time, was the same in all samples. This assumption is justified by two studies. High-precision Sm-Nd geochronology demonstrates that the final time of mineral growth in metapelites from the garnet and sillimanite zones of the type Barrovian locality, Scotland, are the same within error of measurement (Baxter and others, 2002). Measured Th-Pb ages of metamorphic monazite neoblasts in metapelites from the andalusite and sillimanite zones, south-central Maine, are also statistically indistinguishable (Wing and others, 2003). The second assumption cannot be rigorously evaluated, however, until geochronometers are developed that can precisely date mineral reactions in metacarbonate rocks.

The inversion provides estimates of the 3D time-integrated fluid flux vector. Accordingly results cannot distinguish whether flow that drove mineral reaction and isotopic alteration was steady and uniform, continuous but in pulses, or episodic. If flow occurred at various times and in various geometries, the inversion returns a vector that represents an average of the reactive fluid flow geometry.

Mass transport by diffusion and dispersion.—Reversals in gradients of proxies for both X_{CO_2} and $\delta^{18}O_f$ in the Waits River Formation elsewhere in eastern Vermont limit the scale of mass transport by diffusion and hydrodynamic dispersion to between several and several tens of m (Penniston-Dorland and Ferry, 2006). In contrast, mass transport of CO_2 by fluid flow must have occurred over a scale of tens of km or more during regional metamorphism of the Waits River Formation (Ferry, 1992; Penniston-Dorland and Ferry, 2006). Because of the small scale of its effects relative to both the scale of fluid flow and the size of the area in figure 5, as a simplification, mass transport by diffusion and dispersion was not explicitly considered in the inversion (eq 1). The effects of diffusion and dispersion, however, were indirectly considered with the misfit term, e_i, in equation (1).

Reaction kinetics.—Theoretical models of reactive fluid flow in which mineral-fluid reaction is kinetically limited often predict gradients in fluid composition that do not differ significantly from gradients predicted from mineral-fluid equilibrium (for example, Ague, 1998). As a simplification, therefore, gradients in X_{CO_2}, $^{18}O_f$, and $^{13}C_f$ in the area of figure 5 were computed assuming mineral-fluid equilibrium. Although reaction kinetics were not explicitly considered in the inversion (eq 1), they were indirectly considered with the misfit term, e_i.

Constant fluid composition during reaction.—Values of $\delta^{18}O_f$, and $\delta^{13}C_f$ change during the progress of metamorphic dehydration and decarbonation reactions (Rumble, 1982), and X_{CO_2} does as well if mineral reactants and/or products are solid solutions (Ferry and others, 2005; Penniston-Dorland and Ferry, 2006). The predicted changes in C_i during reaction are small relative to the range in C_i over the area of figure 5. As a simplification, therefore, the inversion assumes constant values of C_i during final mineral reaction equal to those recorded by mineral-fluid equilibria. Uncertainties introduced by the simplification were indirectly accounted for by the misfit term, e_i, in equation (1).

Deformation during and following mineral-fluid reaction.—The inversion will return an erroneous characterization of the flow field if there was significant displacement of sample locations relative to each other either during or after metamorphic fluid flow, and if that deformation is not accounted for. Even if deformation involved uniform rotation and/or displacement of the array of sample locations as a whole, the predicted orientation, if not the magnitude, of estimated flow will be in error. The effects of deformation following fluid flow and reaction, in principle, can be explicitly

incorporated in the inversion (Appendix A). In the absence of a detailed history of post-metamorphic deformation in the study area, as a simplification, the inversion assumes that the present geographic distribution of sample locations is the same as that during the time of final mineral reaction during metamorphism.

Geological constraints on the geometry of fluid flow.—The inversion method is sufficiently flexible to include geologic constraints on the geometry of fluid flow. A plausible constraint in the area of figure 5 is layer-parallel flow as is documented by numerous studies of Acadian regional metamorphism in New England (Ferry, 1988, 1994; Kohn and Valley, 1994; Vyhnal and Chamberlain, 1996; Bickle and others, 1997; Ague, 2003; Penniston-Dorland and Ferry, 2006). We chose, however, not to impose any independent geological constraints in order to make an unbiased assessment of the relationship between 3D fluid flow geometry and the orientation of lithologic layering.

Tracer Characteristics at the Time of Final Mineral-Fluid Reaction

The inversion was based on samples from 38 locations in figure 5 (30 real and 8 fictive around the Black Mountain granite). The set of 38 points was gridded according to its Delaunay triangulation, and elements with sides that did not honor the distribution of isograds were removed from the grid. Figure 6 illustrates the final inverse grid (all grid nodes are numbered according to Table 1 of Wing and Ferry, 2002). The grid contains 47 elements, and nodal separations range from 0.3 to 13.6 km with an average of 2.8 km. At each grid point in figure 6, X_{CO_2}, $\delta^{18}O_f$, $\delta^{13}C_f$, and whole-rock changes in CO_2, H_2O, $\delta^{18}O$, and $\delta^{13}C$ were computed with reference to the time of final mineral-fluid reaction (all results in Table 1 of Wing and Ferry, 2002). Average tracer concentration and source values for the three samples collected from the Di zone were assigned to the eight fictive sample locations. Tracer concentration and source term maps (fig. 7) include the fictive data for eight samples in the Di zone (fig. 6).

The X_{CO_2} of the metamorphic fluid was computed from measured mineral compositions (Ferry, 1992), thermodynamic data (Berman, 1988, updated 1992), and estimated P and T, assuming mineral-fluid equilibrium (Ferry, 1992, 1994). Values average 0.04 ± 0.02 (1σ) in the Olig zone, 0.14 ± 0.03 in the Bt zone, 0.20 ± 0.03 in the Amph zone, 0.08 ± 0.01 in the Di zone. The regional distribution of X_{CO_2} broadly resembles the pattern of isograds (fig. 7A). Changes in whole-rock CO_2 contents during final metamorphic mineral reaction were estimated using modes and mineral compositions in equivalent rocks at lower grades, assuming that only H_2O, CO_2, and minor alkalis were lost during metamorphism (Ferry, 1992, 1994). Changes in CO_2 contents were estimated specifically for the transition to the present mineral assemblage from the calculated mineral assemblage of a chemically equivalent rock in the next lower-grade metamorphic zone. For example, estimated changes in CO_2 content for samples in the Di zone represent the difference between the CO_2 content of each sample in the Di zone and the calculated CO_2 content of a chemically equivalent rock in the Amph zone. Estimated whole-rock changes in CO_2 content were corrected for net loss of fluid by calculating $N^*_{CO_2} = [N_{CO_2} - X_{CO_2}(N_{CO_2} + N_{H_2O}]$. Corrections typically were only ≈10 percent. Average values of $N^*_{CO_2}$ are: $2\times10^{-5} \pm 2\times10^{-5}$ (1σ) mol CO_2/cm^3 rock for the Olig zone, $1.2\text{x}10^{-3} \pm 0.9\text{x}10^{-3}$ for the Bt zone, $1.1\times10^{-3} \pm 0.6\times10^{-3}$ for the Amph zone, and $3.4\times10^{-3} \pm 0.3\times10^{-3}$ for the Di zone. The area-weighted average $N^*_{CO_2}$ value for the entire region considered in the inversion, $1.1\times10^{-3} \pm 0.2\times10^{-3}$ (1 standard error, s.e.) mol CO_2/cm^3, confirms that metacarbonate rocks in the Waits River Formation were an open system at that scale (Ferry, 1992). (Calculation of the uncertainty in areal average $N^*_{CO_2}$ is explained in the next section.) Because CO_2 was added to the pore fluid by decarbonation reactions everywhere in the

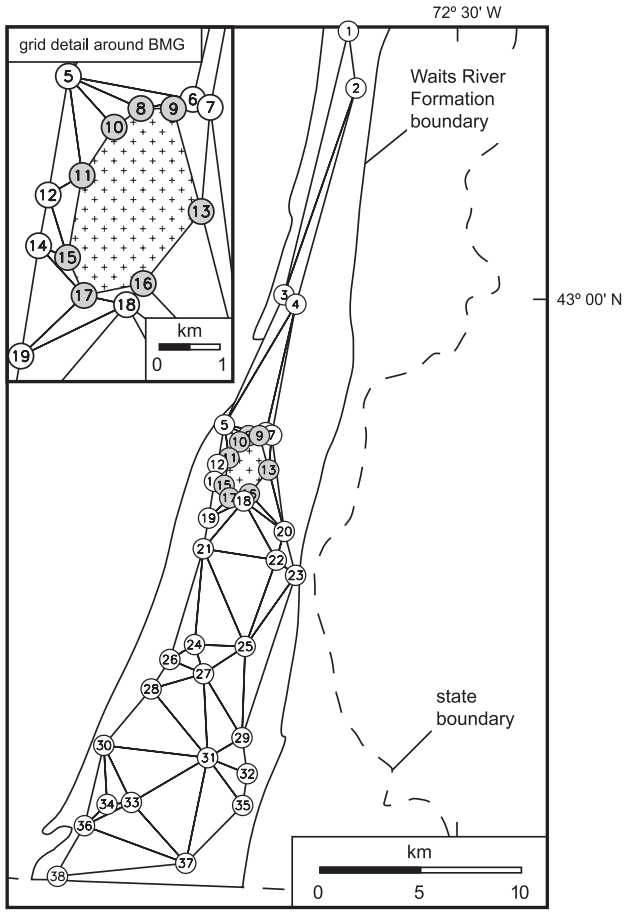

Fig. 6. Finite-element grid used in the field inverse model. Numbers refer to samples listed in Table 1 of Wing and Ferry (2002). The thirty sample locations shown in figure 5 were supplemented by 8 nodes, indicated by gray circles, added around the margin of the Black Mountain granite. Inset details grid at margin of the Black Mountain granite. Grid represents the Delaunay triangulation of all 38 nodes, modified as described in text.

study area (fig. 7B), tracer mass balance requires that fluid flow at the time of final mineral reaction was dominantly in the direction of increasing X_{CO_2}.

Whole-rock and fluid $\delta^{18}O$ and $\delta^{13}C$ values were calculated assuming isotopic exchange equilibrium among minerals and a CO_2-H_2O fluid. Calculations followed procedures in Rumble (1982) and used measured isotopic compositions of carbonate minerals (Stern and others, 1992), mineral modes, estimated temperature recorded by mineral equilibria, and an internally-consistent set of mineral-fluid fractionation factors derived from published studies (Sheppard and Schwarcz, 1970; Matshuhisa and others, 1979; Matthews and others, 1983; Chiba and others, 1989; Chacko and others, 1991; Zheng and others, 1994; Cole and Ripley, 1999). Average calculated $\delta^{18}O_f$ in each zone is: 15.9 ± 1.4 (1σ) permil (V-SMOW) in the Olig zone, 16.1±1.9 permil in the Bt zone, 17.4 ± 1.7 permil in the Amph zone, and 11.6 ± 0.3 permil in the Di zone. Corresponding estimates of average $\delta^{13}C_f$ are: 1.9 ± 1.2 (1σ) permil (V-PDB), 0.4 ± 1.3 permil, 0.6 ± 1.2 permil, and -3.5 ±0.5 permil. Measured O and C isotopic compositions of carbonates are the primary control on the estimated isotopic compositions of

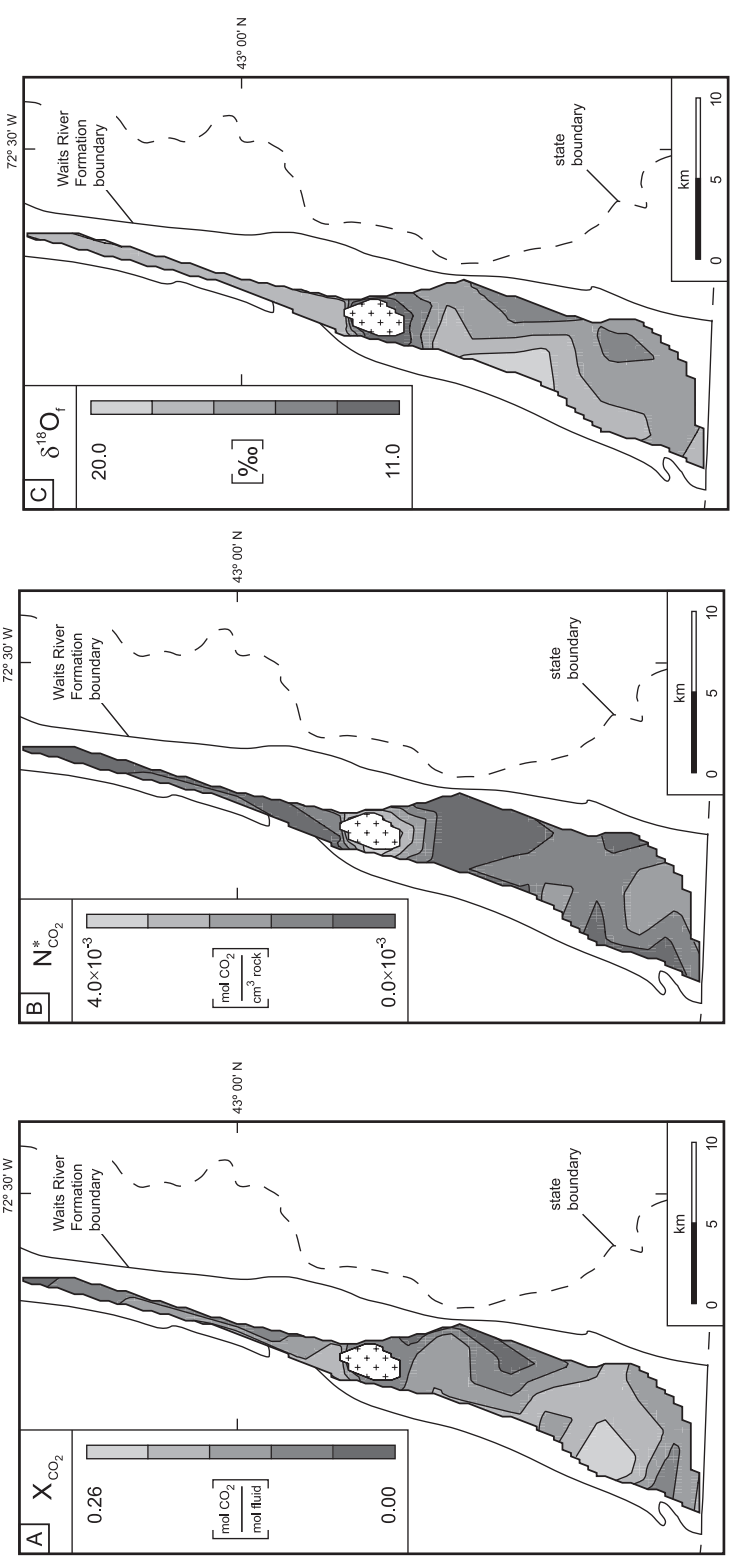

Fig. 7. Tracer concentration and source term data used in inverse model, calculated as described in text. Plots were constructed from the estimated values at each sample location and the linear trial functions used to approximate variability over the finite element grid. Source terms reflect tracers lost from (positive values) or gained by (negative values) rocks during final metamorphic mineral-fluid reaction, and were corrected for the effects of closed system devolatilization as described in text. (A) Contour plot of X_{CO_2} in fluid. (B) Contour plot of effective CO_2 sources. (C) Contour plot of $\delta^{18}O$ in fluid. (D) Contour plot of effective $\delta^{18}O$ sources. (E) Contour plot of $\delta^{13}C$ in fluid. (F) Contour plot of effective $\delta^{13}C$ sources.

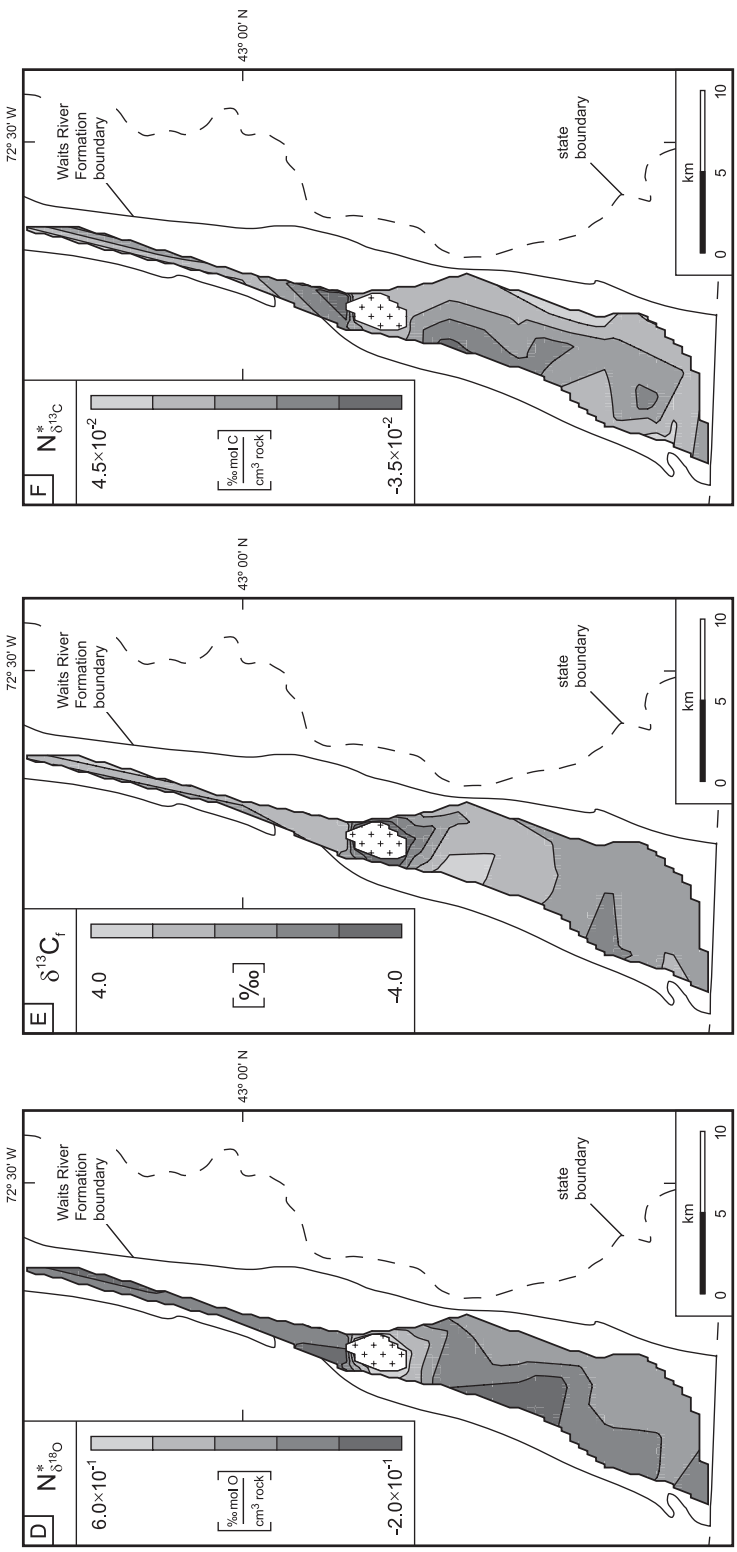

Fig. 7 (continued)

the fluid; modes and temperature variations lead to secondary effects (≈0.1‰ for both O and C). The first-order structure in the mapped pattern of $\delta^{18}O_f$ is a gradual ≈7 permil decrease from the western to the eastern margins of the study area and a region of low $\delta^{18}O_f$ around the Black Mountain granite (fig. 7C; see also Stern and others, 1992). The mapped pattern of $\delta^{13}C_f$ exhibits several local areas of low values, including a distinct halo around the Black Mountain granite (fig. 7E). Regional-scale structure in $\delta^{13}C_f$, however, is not apparent.

Source terms for the isotopic tracers for each sample were estimated similarly as for CO_2 from the change in whole-rock O and C contents (computed from changes in CO_2 and H_2O contents) and the changes in whole-rock $\delta^{18}O$ and $\delta^{13}C$ ($\delta^{18}O_r$ and $\delta^{13}C_r$) at the time of final mineral reaction. Specifically, changes in $\delta^{18}O_r$ and $\delta^{13}C_r$ for each sample were taken as the difference between present values and those inferred for equivalent rocks in the next lower grade zone of metamorphism. Whole-rock $\delta^{18}O$ values for lower-grade equivalents were estimated from the average measured $\delta^{18}O_{carbonate}$ in each zone (Stern and others, 1992) and an empirical correlation between measured $\delta^{18}O_{carbonate}$ and estimated $\delta^{18}O_r$ for analyzed samples in each zone. The resulting small correction (approximately -0.2‰) was applied to average measured $\delta^{18}O_{carbonate}$ values to account for the presence of other O-bearing minerals in lower-grade protoliths. Values of $\delta^{13}C_r$ for lower-grade equivalents were taken as the average of measured $\delta^{13}C_{carbonate}$ in each zone (Stern and others, 1992), assuming all exchangeable C in a rock was in carbonate minerals (justified by data in fig. 7 of Stern and others, 1992). We accounted for the change in $\delta^{18}O_r$ and $\delta^{13}C_r$ in each sample caused by devolatilization by computing N_i^* values. Corrections for the effect of fluid loss generally were ≈10 percent for $\delta^{18}O_r$ in the Olig, Bt, and Di zones; corrections were higher in the Amph zone because of the small calculated changes in $\delta^{18}O_r$. Corrections were <5 percent in the case of $\delta^{13}C_r$ because of the low C content of the fluid.

Average values of $N^*_{\delta^{18}O}$ are: $0.8\times10^{-1} \pm 1.1\times10^{-1}$ (1σ) ‰ mol O/cm^3 rock for the Olig zone, $1.2\times10^{-1} \pm 1.5\times10^{-1}$ for the Bt zone, $-0.3\times10^{-1} \pm 1.5\times10^{-1}$ for the Amph zone, and $5.1\times10^{-1} \pm 0.3\times10^{-1}$ for the Di zone. Average values of $N^*_{\delta^{13}C}$ are: $2.1\times10^{-2} \pm 1.8\times10^{-2}$ (1σ) ‰ mol C/cm^3, $1.8\times10^{-2} \pm 1.9\times10^{-2}$, $-0.7\times10^{-2} \pm 1.7\times10^{-2}$, and $2.3\times10^{-2} \pm 0.5\times10^{-2}$ for the Olig, Bt, Amph, and Di zones, respectively. The area-weighted average $N^*_{\delta^{18}O}$ and $N^*_{\delta^{13}C}$ values for the entire region considered in the inversion are $1.0\times10^{-1} \pm 0.3\times10^{-1}$ (1 s.e.) ‰ mol O/cm^3 rock and $1.1\times10^{-2} \pm 0.3\times10^{-2}$ (1 s.e.) ‰ mol C/cm^3, respectively. (Calculation of the uncertainties in areal average $N^*_{\delta^{18}O}$ and $N^*_{\delta^{13}C}$ is explained in the next section.) Loss of the heavy isotope from rock is indicated by positive values and addition is indicated by negative values. The unusual units for the effective isotopic source terms arise from equation (3) that involves molar changes in whole-rock O and C during metamorphism and isotopic compositions in δ notation. Although average $N^*_{\delta^{18}O}$ and $N^*_{\delta^{13}C}$ values for all zones but the Di zone are not significantly different from zero, significant differences do occur between individual sample locations. Net effective losses of ^{18}O and ^{13}C from the entire study area (areal average $N^*_{\delta^{18}O}$ and $N^*_{\delta^{13}C}$ significantly >0) indicate that isotopic alteration largely reflects a regional process, such as fluid flow, rather than a purely local thermally-controlled process, such as closed-system devolatilization. The mapped pattern of $N^*_{\delta^{18}O}$ is smooth and regular (fig. 7D) compared to that of $N^*_{\delta^{13}C}$ (fig. 7F) which is variable on a scale similar to the characteristic length scale of the underlying grid (≈3 km). Additional processes controlling C isotopic alteration besides fluid flow therefore may have operated at a comparable or smaller spatial scale.

Preparation of Data for Inversion

Isotopic compositions of the metamorphic fluid were converted from δ to C_i values by incorporating conservation of total O and C in the metamorphic fluid through equation (2). The distribution of these quantities and X_{CO_2} on the inverse

grid provided the horizontal tracer gradients required for the inverse technique. Through the finite element methods, we estimated the horizontal tracer gradient at each node through linear interpolation of the C_i values defined at each node.

Hydrodynamic models of metamorphism universally predict a significant component of fluid flow in the vertical dimension (for example, Hanson, 1992, 1995, 1997; Gerdes and others, 1995; Connolly, 1997; Cui and others, 2003). It is essential, therefore, to constrain tracer gradients in the vertical dimension as well as horizontal dimensions if the inversion is to return a meaningful estimate of the 3D geometry of metamorphic fluid flow. Because there is very little topographic relief in the area of figure 5, tracer gradients in the vertical dimension z ($(\partial C_i/\partial z)$, z coordinate positive upward) were approximated from tracer gradients in the horizontal dimensions. First, the value of normalized temperature $T' = (T_{sample}\text{-}T_{Olig})/(T_{Di}\text{-}T_{Olig})$ was computed for each sample location where subscripts refer to the sample, average T in the Olig zone, and average T in the Di zone. Second, the direction of maximum decrease in T' in the horizontal dimension was determined for each element of the grid from the spatial distribution of T' on the inverse grid. Third, the gradient in C_i for each tracer along that direction was computed from the dot product of the direction of maximum decrease in T' with the horizontal tracer gradient. For elements formed by three samples of equal T', the tracer gradient in the direction of maximum decrease in T' was assumed to be equal to the average of corresponding tracer gradients from all adjoining elements. Finally, a normal geothermal gradient at the time of final mineral reaction during metamorphism was assumed (decreasing T with decreasing depth), and $\partial C_i/\partial z$ for each element of the grid was assigned the value of the gradient in C_i along the horizontal direction of maximum decrease in T'. These estimates essentially assume that variations in temperature during metamorphism in the vertical dimension were comparable to maximum variations in temperature in the horizontal dimensions. Although the assumption may not be appropriate for all regional metamorphic terrains, it is likely a good one for the study area considering that isograds are unusually closely spaced in both metacarbonate rocks (fig. 5) and pelites. For example, the transition from the chlorite to kyanite zones in pelites can occur over horizontal distances <2 km (Hepburn and others, 1984). Because of how values of $\partial C_i/\partial z$ were estimated, the inversion is best interpreted as the flux field for a thin shell within the crust. The assumption of a normal rather than an inverted geothermal gradient is addressed in a later section.

Monte Carlo resampling of the N_i^* values for each tracer provided estimates of the acceptable misfit in the inversion. The areal average value of $N^*_{CO_2}$, 1.07×10^{-3} mol CO_2/cm^3 rock, was computed from dividing the integration of $N^*_{CO_2}$ over the area of the inversion (fig. 7B) by the total area of the inversion. We repeated this procedure for each of the resampled datasets (eq 7), producing a near Gaussian bootstrap distribution with mean $N^*_{CO_2}$ of 1.10×10^{-3} mol/cm^3 (fig. 8A). The standard error of the Monte Carlo estimate of the mean is 0.18×10^{-3} mol/cm^3. The areal average of $N^*_{\delta^{18}O}$ (fig. 7D), computed similarly, is 1.01×10^{-1} ‰ mol O/cm^3 rock. The bootstrap distribution of the resampled source terms is nearly Gaussian and has a mean $N^*_{\delta^{18}O}$ of 1.24×10^{-1} ‰ mol/cm^3 with a standard error of 0.34×10^{-1} ‰ mol/cm^3 (fig. 8B). The calculated areal average of $N^*_{\delta^{13}C}$ (fig. 7E) is 1.11×10^{-2} ‰ mol C/cm^3 rock, while the resampling procedure returned a nearly Gaussian bootstrap distribution with a mean of 1.58×10^{-2} ‰ mol/cm^3 and a standard error of 0.34×10^{-2} ‰ mol/cm^3 (fig. 8C). The Gaussian form of all three bootstrap distributions largely reflects the procedure of areal averaging, and illustrates the effect of the central limit theorem.

The areal average $N^*_{CO_2}$ calculated from the measured dataset is only 3 percent smaller than the bootstrap estimate from the resampled datasets. Areal averages from the measured isotopic source terms, however, are less than their bootstrap equivalents

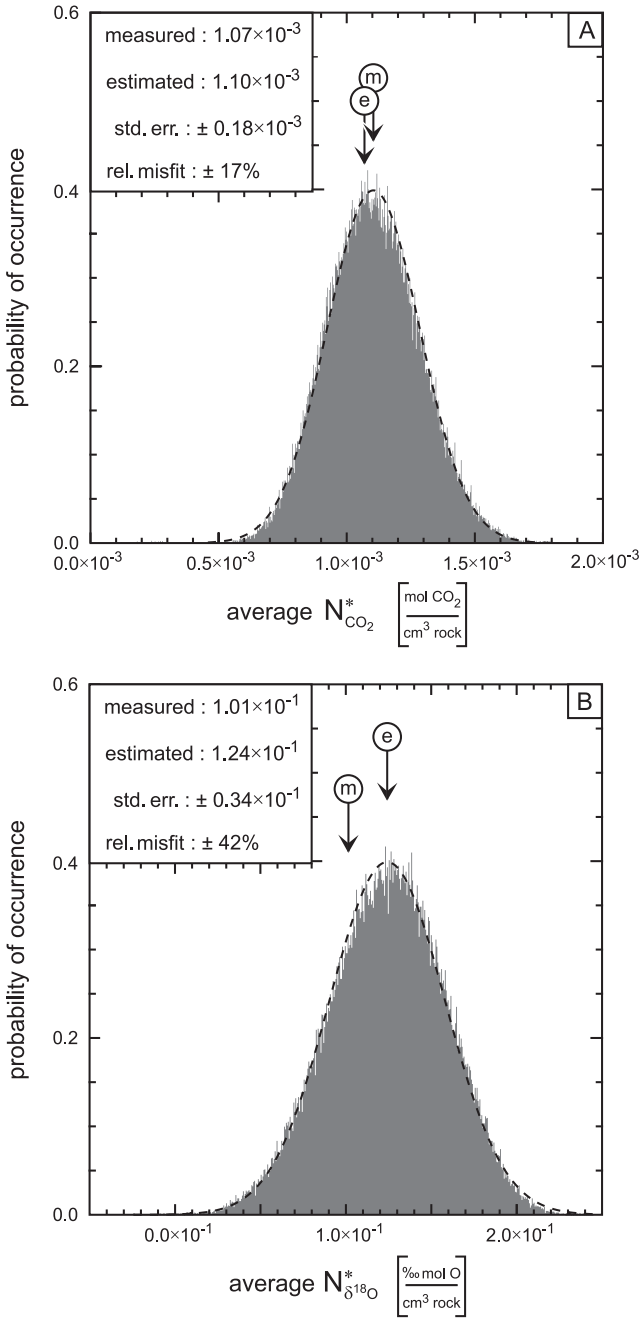

Fig. 8. Uncertainty estimates for tracer source terms in inverse model. On each histogram (gray), "m" represents the areally-averaged measured effective tracer change in the rock over the area of figure 7 calculated from the actual sample set, and "e" represents the Monte Carlo estimate of the tracer change. Standard deviation is estimated from the Gaussian approximation to the histogram (dashed curve). The difference between "m" and "e" indicates the bias in the Monte Carlo estimation procedure, and provides a first-order correction to the standard deviation. Calculation of acceptable misfit, $\sigma_{N_i}^*$, accounts for this bias as described in the text. (A) Histogram of average CO_2 source. (B) Histogram of average $\delta^{18}O$ source. (C) Histogram of average $\delta^{13}C$ source.

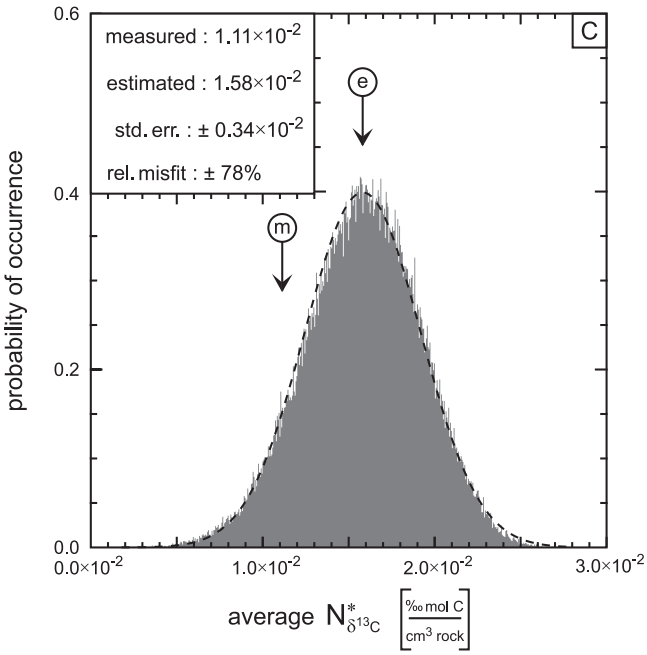

Fig. 8 (continued)

by 19 percent for $N^*_{\delta^{18}O}$ and 30 percent for $N^*_{\delta^{13}C}$. The inverse grid appears to provide enough resolution to eliminate almost all bias when resampling for CO_2 sources but not when resampling for isotopic sources. We applied a first-order correction for bias between the measured and bootstrap average source terms by first taking the ratio of the probabilities of the bootstrap and measured average source terms (that is, where the arrows marked "e" and "m" intersect the dashed curves in fig. 8), and then shifting the peak of the bootstrap probability distribution to the measured average source term (that is, centering the dashed curve on the arrow marked "m"). The relative standard deviation of the resulting distribution (that is, the standard deviation of the bootstrap distribution divided by the measured average source term) was multiplied by the probability ratio to calculate a relative misfit. The practical effect of this correction was to increase the misfit allowed in the inversion. Estimated relative misfits were 18 percent for $N^*_{CO_2}$, 42 percent for $N^*_{\delta^{18}O}$, and 78 percent for $N^*_{\delta^{13}C}$. Acceptable misfits for the source terms ($\sigma_{N_i^*}$ in eq 9) at each node were taken as the larger of either the product of the relative misfit with the source term at that node or the standard error of the bootstrap estimate. This approach allowed for greater source-term variability where alteration was most intense, while setting a firm lower limit on the amount of variability at each node.

Magnitude and 3D Geometry of Metamorphic Fluid Flux

Calculated results.—An inversion based on all CO_2, $\delta^{18}O$, and $\delta^{13}C$ data returned a time-integrated metamorphic fluid flux field that was not spatially uniform in either magnitude or direction. Specifically, the inversion returned a wide range of values of time-integrated fluid flux at individual nodes, ranging by more than a factor of 30 from 1×10^4 to 3.3×10^5 mol fluid/cm^2 rock. The components of the flux vector at each node are likewise widely variable with values ranging from -2.0×10^5 to 1.4×10^2 mol/cm^2 in the x direction (E-W, positive to the E), -1.2×10^5 to 1.5×10^5 mol/cm^2 in the y direction (N-S,

positive to the N), and -6×10^4 to 2.7×10^5 mol/cm^2 in the z direction (vertical, positive upward). Uncertainties in flux components at each node are highly correlated and have standard errors that are the same order of magnitude as the fluxes themselves. The estimated area-weighted average time-integrated flux vector is resolved into components $-1.8\times10^4 \pm 0.8\times10^4$ (1σ) mol/cm^2 in the x direction, $-0.5\times10^4 \pm 1.0\times10^4$ mol/cm^2 in the y direction, and $1.2\times10^4 \pm 0.8\times10^4$ mol/cm^2 in the z direction. The magnitude of the areal average time-integrated fluid flux vector, $2.2\times10^4 \pm 1.5\times10^4$ mol/cm^2, falls within the range of estimates based on both the devolatilization budget of regional metamorphic terrains and on local transport models for metamorphic fluid flow (Walther and Orville, 1982; Baumgartner and Ferry, 1991; Stern and others, 1992; Ferry, 1992, 1994; Léger and Ferry, 1993; Skelton and others, 1995; van Haren and others, 1996; Hanson, 1997; Evans and Bickle, 1999; Ague, 2004).

Regional patterns of fluid flow in 3D.—Because of the uncertainties in the estimated time-integrated fluid flux vectors at each node, the inverse solution is in a regime like the inversion of synthetic data illustrated in figure 4. The actual flux field at the time of final mineral reaction during metamorphism was probably only broadly similar to the inverse flux field. Bearing this in mind, the regional pattern of time-integrated fluid flux was computed using a linear interpolation of the inverse model onto a regular grid (fig. 9). The large variability in estimated time-integrated flux between individual nodes is damped by the interpolation procedure. The area in figure 9 can be separated into three regions based on the mapped pattern of time-integrated flux. From the northern limit of the study area to ≈2 to 3 km south of the Black Mountain granite, flux vectors are directed towards the granite with a strong upward component at the margin of the pluton. Most flux vectors south of this area to ≈5 km north of the southern margin of the study area are nearly horizontal and directed toward the center of the terrain. In the southernmost part of the area, flux vectors diverge upward and outward from the southeastern corner of the study area. These general patterns were preserved in all inversions along the "knee" of the trade-off curve (Parker, 1977).

Consideration of an inverted geothermal gradient.—Because of the significant difference in P-T conditions recorded by mineral equilibria in rocks from eastern Vermont and in those from western New Hampshire, hot nappes, whose remnants are preserved in western New Hampshire, may have covered rocks in eastern Vermont during Acadian regional metamorphism (Spear and others, 2002). It is possible then that the geothermal gradient was inverted during metamorphic fluid flow in the study area. The effect of an inverted geothermal gradient on the estimated time-integrated flux field returned by the inversion can be easily evaluated. The inverse method is applied to a linear set of time-integrated mass balance equations with coefficients in the z direction defined by the assumed local vertical temperature gradient. If the vertical temperature gradients were of the same magnitude as the ones considered in the inversion but of the opposite sign (inverted), a new inversion therefore would return the same flux components in the horizontal dimensions and flux components in the vertical dimension of the same magnitude but in the opposite direction. With an inverted geotherm, the areal average time-integrated fluid flux vector would be directed downward rather than upward. Regions of downward-directed fluid flow in figure 9 would become regions of upward-directed flow and the regions of upward-directed flow would become regions of downward-directed flow. The magnitude of the vectors in figure 9 would remain unchanged.

Consideration of devolatilization in interbedded pelitic schists.—Because the Waits River Formation is composed of interbedded pelitic schist and metacarbonate rock, a second inversion was performed that explicitly accounted for devolatilization reactions in both rock types. Because there are no systematic data on mineral-fluid equilibria, stable isotope compositions, and mineral reaction progress for pelitic rocks in the study area,

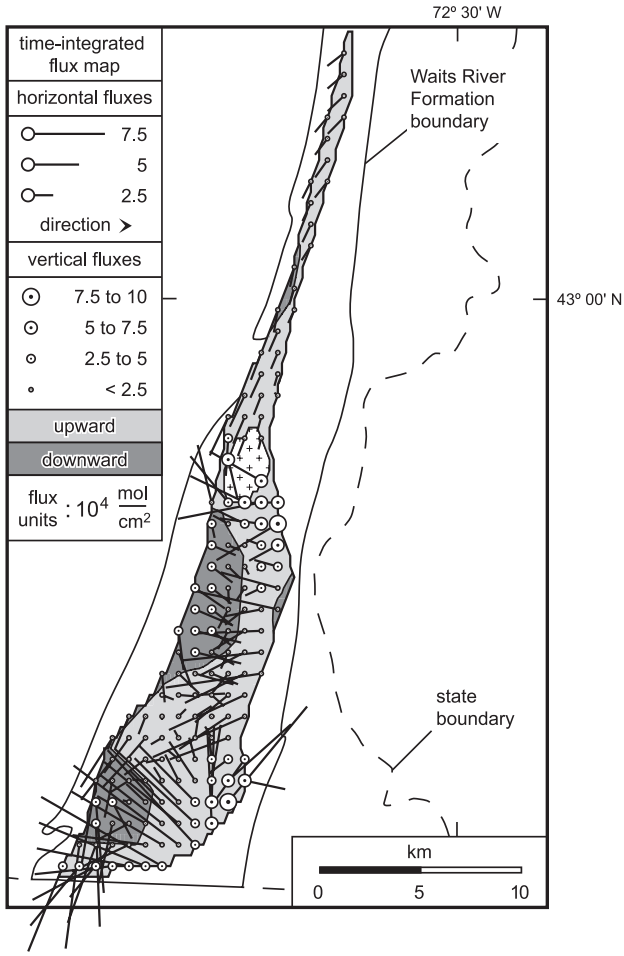

Fig. 9. Map of three-dimensional time-integrated fluid flux predicted from field inverse model. Direction and magnitude of horizontal fluxes are represented by direction and length of thick black lines and of vertical fluxes by size of circles and shading. Although the inverse model considered data from only metacarbonate rocks in the Waits River Formation, quantitative consideration of the additional effects of interbedded pelitic schists leads to essentially the same flux patterns (Wing and Ferry, 2002).

behavior of the pelitic schists during metamorphism could only be approximately specified. Devolatilization of pelites was inferred using Shaw's (1956) average composition of low-grade pelite and representative devolatilization reactions observed in pelites elsewhere in eastern Vermont (Ferry, 1988, 1994). Zero values of $N^*_{\delta^{18}O}$ and $N^*_{\delta^{13}C}$ were assigned to the pelites. Results of the second inversion were reported elsewhere (Wing and Ferry, 2002). The areal average time-integrated flux vector diverges by ≈10° from and is ≈25 percent smaller in magnitude than the corresponding areal average vector returned by the inversion that considers data only from the metacarbonate rocks. Differences between the mapped patterns of time-integrated fluid flux based on an inversion that considers both metacarbonates and pelites and those fluxes shown in figure 9 are barely discernable at the scale of the figure.

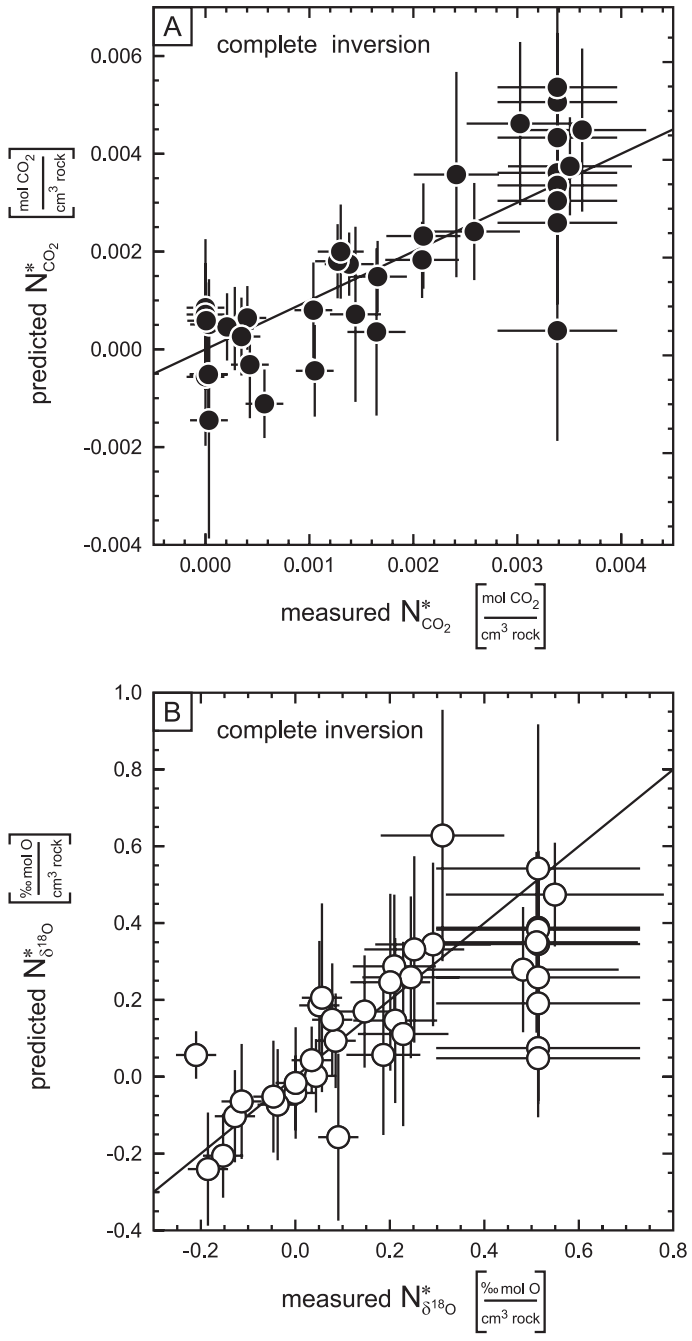

Fig. 10. Comparison of predicted and measured effective tracer source terms for full inversion of CO_2, $\delta^{18}O$, and $\delta^{13}C$ data. In all plots, thin continuous line in background represents one-to-one correspondence and horizontal (vertical) lines behind symbols represent *a priori* (*a posteriori*) uncertainty estimates. (A) Comparison of predicted and measured CO_2 sources. (B) Comparison of predicted and measured $\delta^{18}O$ sources. (C) Comparison of predicted and measured $\delta^{13}C$ sources.

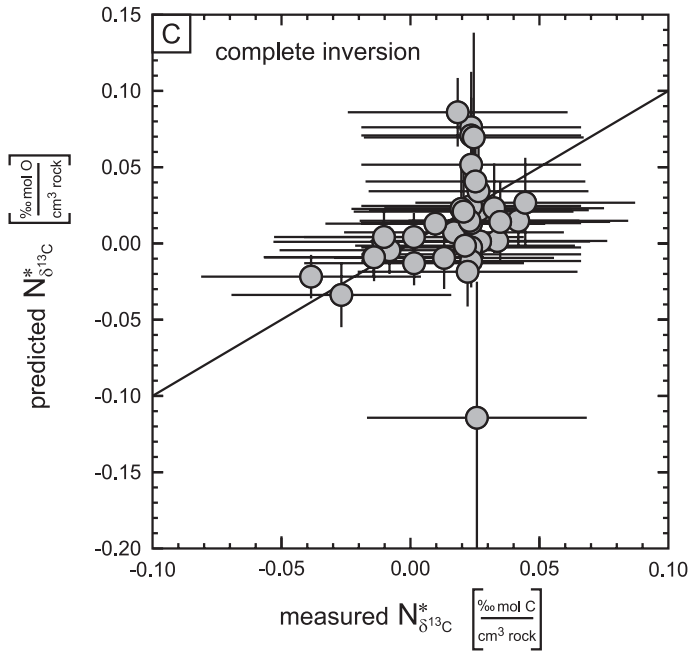

Fig. 10 (continued)

Misfit and Consistency

We evaluated the performance of the inversion by comparing measured source terms at each node with those predicted from the inverse estimate of fluxes (fig. 10). The vertical distance between each point and the 1:1 lines in figure 10 is the actual misfit in the inversion while the horizontal lines behind each point represent the misfit that was accepted in each source term at the start of the inversion. The reduced chi-squared statistic requires that the two misfits match when averaged over the three tracers from all samples. We evaluated the tracer mass balance equations with the inverse flux field to predict source terms for each tracer. Uncertainty estimates for predicted values of source terms (vertical lines behind each point in fig. 10) resulted from propagation of flux uncertainties through equation (6). Because the inversion was based on data for all three tracers, its predictions generally reproduced the measured source term values within the uncertainties of measurement and prediction.

Comparison of measured with predicted tracer source terms makes clear that CO_2, and to a lesser extent $\delta^{18}O$, controlled the results of the inversion (figs. 10A and 10B). Acceptable misfits for $\delta^{13}C$ were large enough (fig. 10C) that it was effectively 'diagnostic' (Wunsch, 1996), and contributed little weight to the least squares functional (eq 8), the final chi-square sum (eq 9), and, accordingly, the inverse solution. While a diagnostic tracer does not constrain the inverse flux field, it can be used to evaluate the validity of the inversion. In this sense, the inversion in figure 9 was dominantly a two-tracer inversion (CO_2 and $\delta^{18}O$) that produced a result consistent with data for a third, $\delta^{13}C$ (fig. 10C).

In addition, by setting the acceptable relative misfit for $\delta^{18}O$ and $\delta^{13}C$ to an artificially large value ($\approx 10^5$), we examined an inverse solution that depended only on CO_2. The inversion based on only CO_2 data predicted $\delta^{18}O$ and $\delta^{13}C$ sources that were of the same order of magnitude as measured sources, but differed in detail from the

measured sources. Analogous inversions based on only $\delta^{18}O$ or only $\delta^{13}C$ data, however, failed to predict CO_2 sources that were even of the same order of magnitude as measured sources. The consistency tests indicate that the basic structure of the time-integrated flux field is primarily controlled by constraints of CO_2 conservation. Because they act as 'anomaly' tracers (Wunsch, 1996), isotopic data provide information about flux variability around the inverse model derived from CO_2 conservation.

Resolution Tests

In contrast to the perfectly known synthetic data set, field data consist of a limited number of tracer measurements of imperfect accuracy. As a result, the inversion of a set of field tracer measurements cannot fully resolve the features of the underlying flux field. The degree of resolution that a particular inversion provides is case-specific and is determined primarily by the density and coverage of the input data. We adapted a checkerboard resolution test commonly used in inversions of seismic data (for example, West and others, 2001; Tilmann and others, 2003) to estimate the resolving power of the inverse model for the field application in southeastern Vermont.

The average length scale of the underlying grid (≈3 km) sets an approximate lower limit of the spatial resolution of the inverse model. Processes or features smaller than this scale cannot be resolved. This estimate does not take into consideration any local structure in the data, and does not account for the mass balance relationships between inverse input (that is, C_i, N_i^*) and inverse output ($\mathbf{q}$). Flux estimates, like the results of any discrete inverse calculation (Backus and Gilbert, 1970), represent localized averages over a subset of the input data and sample locations. We took an empirical approach to determine the size of this averaging region.

The procedure compares an imposed ("true") flux field with an inverse estimate of the imposed field. Synthetic N_i^* values were calculated from field gradients in C_i by imposing time-integrated fluxes in a checkerboard pattern. The flux variation within each cell was defined by a Gaussian vertical flux distribution in the map plane and zero x and y fluxes. Vertical fluxes in alternating cells had alternating signs. An inverse time-integrated flux field was calculated from the synthetic set of N_i^* values and the measured C_i values. The number of checkerboard cells in the x and y directions was varied independently, and the correlation between the inverse flux and the imposed fluxes for each different flux pattern calculated. When the correlation between the imposed field and the inverse field broke down, the area of the associated checkerboard cell provided an empirical estimate of the characteristic size of features that could be resolved by the inverse technique.

Figure 11A shows a representative 3 by 3 checkerboard of an imposed "true" flux field. Because of the discrete nature of the inverse grid, it is not possible to represent this field exactly. We sampled the field at each node and varied the field linearly among nodes (fig. 11B). Inverse flux fields were geometrically similar to the corresponding resampled "true" field with a diminution of the peak flux magnitudes (figs. 11B and 11C). Diminished peak values are a direct result of the smoothness constraint used to regularize the solution. Horizontal flux components are not shown in figure 11C, but they were small and within uncertainty of zero in all inversions.

Correlation between the "true" flux field and the inverse field with increasing number of cells closely followed the correlation between the resampled actual field and the inverse field until a level of ≈80 percent. Here, the "true" and inverse correlation exhibited a sharp decline (fig. 12) while the resampled and inverse correlation remained ≈80 percent. We used 80 percent as the cut-off value for deciding whether or not the "true" and inverse flux fields were correlated. The smallest flux footprint that could be adequately resolved was ≈5 km in the x direction by ≈14 km in the y direction (figs. 11 and 12A). Most of the regional features in the inversion of field data are approximately this size (compare fig. 9 with fig. 11C). This

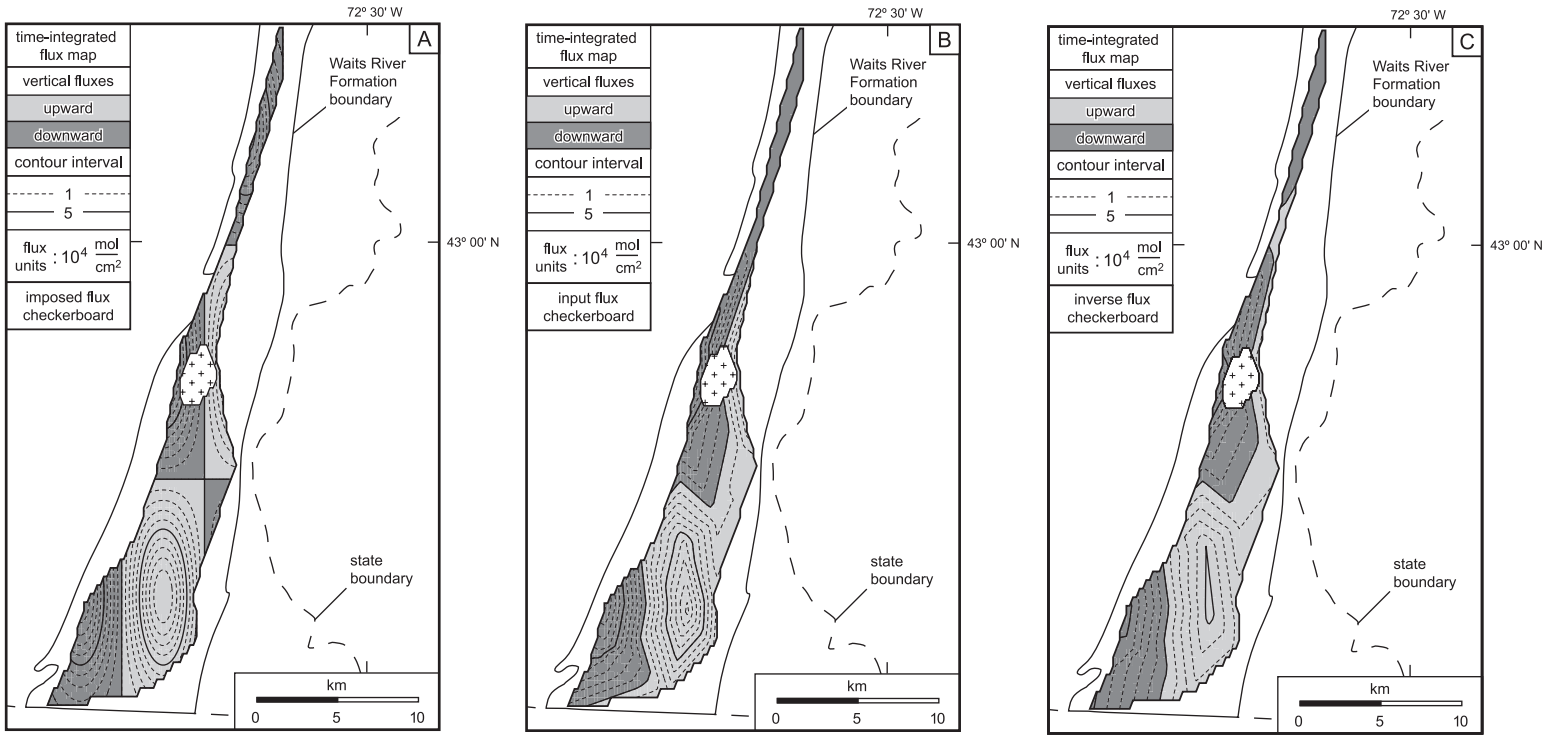

Fig. 11. Representative comparison of imposed, input, and inverse fluxes used for resolution test of field inverse model. In all plots, shading represents vertical direction of flux (light = up, dark = down). Contours represent flux magnitudes. (A) Imposed "true" Gaussian flux checkerboard of 3 cells in x direction versus 3 cells in y direction. (B) Input flux checkerboard. Plot represents flux shown in figure 11A sampled at nodes of grid shown in figure 6 and varying according to the linear trial functions used in the finite element method. A "perfect" inversion could predict imposed flux only as well as the flux map shown here. (C) Inverse flux checkerboard. Plot represents results of inversion completed with measured tracer concentration data and effective tracer source term data calculated from flux field shown in figure 11B. Overall geometry of flux shown in figure 11B is preserved but peak variability is diminished because of regularization of the inverse model.

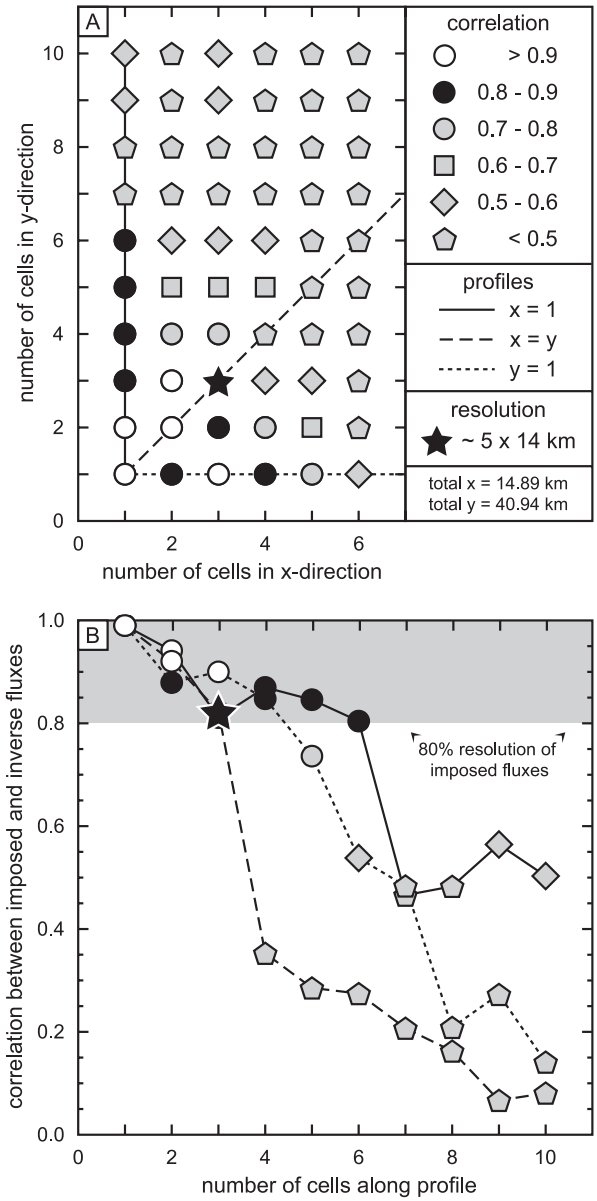

Fig. 12. Comparison of resolution tests of inverse model. (A) Correlation between imposed flux field and inverse flux field as a function of size of checkerboard cells. Symbols indicate degree of correlation. Lines in background correspond to profiles in figure 12B. Star shows conditions of resolution test illustrated in figure 11 and represents maximum resolution considered possible in field inversion. (B) Correlation between imposed flux field and inverse flux field along three paths through figure 12A. Continuous line connects resolution tests where only the number of cells in the y direction was varied. Long dashed line connects resolution tests where the number of cells in both the x and y directions was varied in unison. Short dashed line connects resolution tests where only the number of cells in the x direction was varied. Gray shading indicates region where correlation between imposed and inverse fluxes is considered acceptable (>80%). The checkerboard cell with the smallest area in the family of acceptable resolution tests occurs where the long dashed line intersects with the bottom of the gray band, indicated by a star, and defines the preferred estimate of the resolution of the inverse model.

correspondence indicates that the inverse model provides enough resolving power for a general interpretation of the magnitude and geometry of the metamorphic flux field in the study area.

Regional Fluid Transport During Barrovian Metamorphism, Southeastern Vermont

Resolution tests suggest that the inverse model captures regional-scale features of the flux field at the time of final mineral reaction. The average terrain-scale time-integrated flux vector has a magnitude of $2.2\times10^4 \pm 1.5\times10^4$ (1σ) mol fluid/cm^2 rock, trends 255° in the map plane, and is directed upward at 32° to the horizontal. The average flux vector lies almost exactly in the plane defined by the average orientation of lithologic layering on a regional scale (Wing and Ferry, 2002). Flow at the time of final mineral reaction was apparently largely parallel to stratigraphic contacts whose orientations are controlled by the regional structure in southeastern Vermont.

On average, flux in the study area was directed upward, toward shallower crustal depths, with a component of flux in the z direction of $1.2\times10^4 \pm 0.8\times10^4$ mol/cm^2. Over the whole of the 120 km^2 terrain, this vertical flux was dominantly balanced by the total fluid transported into the study area normal to the outer boundary of the inverse grid ($\approx1.7\times10^{11}$ mol through a 93 km boundary), with minor contributions from fluid produced by rocks inside the grid ($\approx2\times10^8$ mol) and from fluid sourced in the Black Mountain granite and transported into the study area normal to the inner grid boundary ($\approx5\times10^8$ mol across an 8 km boundary). An approximate balance between the total amount of fluid lost from rocks in the study area and the divergence of time-integrated fluid flux through the terrain implies that the vertical flux increased with increasing z (decreasing depth) at a rate of 0.14 ± 0.09 (1σ) mol/cm^3 ($(\partial q_z/\partial \mathbf{z}) \approx$ 0.14 mol/cm^2/cm). Linear extrapolation along this gradient to the crustal level where the vertical flux becomes zero indicates that the base of the flow system was ≈0.5 to 2 km below the present surface. Vertical flux at the present level of exposure could have been totally compensated by the flux entering the terrain horizontally over this depth range. The metamorphic flow system apparently "turned up" just below the present level of exposure, and is largely sourced by fluids originating east of the study area.

Recent tectonic models document significant compressional structures to the east of the study area that were active during the time of metamorphism in eastern Vermont (Spear and others, 2002). Fluids may have been driven westward during compression and deflected upward through the rocks of the Waits River Formation by structurally-focused flow. Upward flow parallel to gross structure in eastern Vermont may have been enhanced by buoyancy induced by thermal highs within structural domes. The inferred flow geometry is consistent with decarbonation reactions driven by flow in the direction of increasing temperature if isotherms in the study area dipped more steeply than ≈30° to the east; more shallowly dipping isotherms could have occurred further to the east where flow was primarily horizontal. As is the case elsewhere in eastern Vermont, fluid flow directly associated with granitic plutons appears to be orders of magnitude less significant than regionally pervasive flow (Léger and Ferry, 1993).

ACKNOWLEDGMENTS

We thank Tom Haine for guidance in inverse theory and practice; Jay Ague, Lukas Baumgartner, and Greg Dipple for discussions on the limits of the inverse approach; and Rainer Abart, Mike Bickle, and Peter Nabelek for patient, thoughtful, and constructive reviews. Research supported by National Science Foundation grants EAR-9805346 and EAR-0229267. The manuscript in part was prepared while BAW received support from National Aeronautics and Space Administration grant NAG-512350 to James Farquhar.

Appendix A

Development of Time-integrated Tracer Transport Equations Used in the Inversion Methods

For a deformable, porous medium with fluid-filled pores, the conservation equations for the total fluid (A1), total solid (A2), tracer species i in the fluid (A3), and tracer species i in the solid (A4) are:

$$\frac{\partial}{\partial t}(\rho_f \phi) = -\nabla \cdot (\rho_f \phi \mathbf{v}) + r_f, \tag{A1}$$

$$\frac{\partial}{\partial t}[\rho_s(1-\phi)] = -\nabla \cdot [\rho_s(1-\phi)\mathbf{V}] - r_f, \tag{A2}$$

$$\frac{\partial}{\partial t}(c_{i,f}\rho_f \phi) = \nabla \cdot (\rho_f \phi \mathbf{D} \nabla c_{i,f}) - \nabla \cdot (c_{i,f}\rho_f \phi \mathbf{v}) + r_{i,f}, \tag{A3}$$

$$\frac{\partial}{\partial t}[c_{i,s}\rho_s(1-\phi)] = -\nabla \cdot [c_{i,s}\rho_s(1-\phi)\mathbf{V}] - r_{i,f}, \tag{A4}$$

where ρ_f is the molar density of the fluid, ϕ is the porosity of the bulk medium, $\mathbf{v}$ is the pore fluid velocity, r_f is the molar transfer rate of total volatiles due to mineral-fluid reaction (positive from the solid to the fluid and negative from the fluid to the solid), ρ_s is the molar density of the solid, $\mathbf{V}$ is the solid velocity, $c_{i,f}$ is the molar abundance of tracer species i in the fluid, $\mathbf{D}$ is the hydrodynamic dispersion tensor, $r_{i,f}$ is the molar transfer rate of tracer species i due to mineral-fluid reaction, and $c_{i,s}$ is the molar abundance of tracer species i in the solid (compare Ague and Rye, 1999; Spiegelman and others, 2001). Notation used throughout the appendices is defined in table A1.

A reduced set of governing equations is required in order to relate field measurements to basic transport quantities. The reduction proceeds in three steps. First, the general governing equations for solid mass conservation are transformed to reflect a geochemical, rock-based reference frame. Second, fluid transport quantities are consolidated to focus on essential aspects of mass transfer. Lastly, the resulting equations are combined and integrated with respect to time.

Field-based estimates of mass loss or gain by a rock during alteration require a geochemical reference frame (compare Brimhall, 1979; Baumgartner and Olsen, 1995; Ague and van Haren, 1996; Breeding and Ague, 2002; Ague, 2003). In a geochemical reference frame, estimates of mass loss or gain by a rock are quantitatively represented by the material derivative for the solid,

$$\frac{D_s h}{Dt} = \frac{\partial h}{\partial t} + \mathbf{V} \cdot \nabla h, \tag{A5}$$

that expresses the rate of change of the quantity of interest, h, observed in a reference frame moving with the solid. With this notation, the solid mass and tracer conservation expressed in equations (A2) and (A4), become respectively,

$$\frac{D_s}{Dt}[\rho_s(1-\phi)] = -\rho_s(1-\phi)\nabla \cdot \mathbf{V} - r_f, \tag{A6}$$

$$\frac{D_s}{Dt}[c_{i,s}\rho_s(1-\phi)] = -c_{i,s}\rho_s(1-\phi)\nabla \cdot \mathbf{V} - r_{i,f} \tag{A7}$$

These equations assign any change in the mass of tracer species i in a unit volume of rock to deformation-induced volume changes and to mass transfer between the solid and fluid by chemical reaction.

Tracer transport during fluid-rock reaction involves both advection and hydrodynamic dispersion. In detail, these processes depend on properties of the moving fluid and on physical characteristics of the rock matrix. By considering total advective and dispersive fluxes, however, detailed dependencies can be ignored. The total tracer flux due to fluid advection, $\mathbf{J}_{i,a}$, is:

$$\mathbf{J}_{i,a} = c_{i,f}\mathbf{u} = c_{i,f}\rho_f \phi \mathbf{v}, \tag{A8}$$

where $\mathbf{u}$ is molar fluid flux. The total tracer flux due to dispersion across a unit area of porous rock, $\mathbf{J}_{i,d}$, is:

$$\mathbf{J}_{i,d} = -\rho_f \phi \mathbf{D} \nabla c_{i,f}, \tag{A9}$$

TABLE A1

Notation and definitions of variables used in appendices

Variable	Description	Units*
ρ_f	molar fluid density	$\left[\frac{\text{mol fluid}}{\text{cm}^3\ \text{fluid}}\right]$
ρ_s	molar solid density	$\left[\frac{\text{mol solid}}{\text{cm}^3\ \text{solid}}\right]$
ϕ	porosity	$\left[\frac{\text{cm}^3\ \text{fluid}}{\text{cm}^3\ \text{bulk}}\right]$
$\mathbf{v}$	pore fluid velocity	$\left[\frac{\text{cm}}{\text{s}}\right]$
$\mathbf{V}$	solid velocity	$\left[\frac{\text{cm}}{\text{s}}\right]$
r_f	molar transfer rate from solid to fluid due to chemical interaction	$\left[\frac{\text{mol fluid}}{\text{cm}^3\ \text{bulk s}}\right]$
$c_{i,f}$	molar abundance of tracer species i in the fluid	$\left[\frac{\text{mol i}}{\text{mol fluid}}\right]$
$c_{i,s}$	molar abundance of tracer species i in the solid	$\left[\frac{\text{mol i}}{\text{mol solid}}\right]$
$r_{i,f}$	molar transfer rate of tracer species i from solid to fluid due to chemical interaction	$\left[\frac{\text{mol i}}{\text{cm}^3\ \text{bulk s}}\right]$
$\mathbf{D}$	hydrodynamic dispersion tensor	$\left[\frac{\text{cm}^2}{\text{s}}\right]$
$\mathbf{u}$	molar fluid flux	$\left[\frac{\text{mol fluid}}{\text{cm}^2\ \text{bulk s}}\right]$
$\mathbf{J}_{i,a}$	advective tracer flux of species i	$\left[\frac{\text{mol i}}{\text{cm}^2\ \text{bulk s}}\right]$
$\mathbf{J}_{i,d}$	dispersive tracer flux of species i	$\left[\frac{\text{mol i}}{\text{cm}^2\ \text{bulk s}}\right]$
$\mathbf{q}$	time-integrated molar fluid flux	$\left[\frac{\text{mol fluid}}{\text{cm}^2\ \text{bulk}}\right]$
S	scale ratio in simple model for fluid flow	dimensionless
$\overline{k_x}$	representative permeability in x direction	cm^2
$\overline{k}_z$	representative permeability in z direction	cm^2
D	vertical scale of material variation in simple model for fluid flow	cm

Table A1
(continued)

Variable	Description	Units*
L	characteristic distance over which D varies	cm
Ra	Rayleigh number in simple model for fluid flow	dimensionless
α	normalized thermal expansivity	$\left[\frac{1}{^{\circ}C}\right]$
g	gravitational acceleration	$\left[\frac{cm}{s^2}\right]$
$\frac{\partial T}{\partial z}$	representative geothermal gradient in simple model for fluid flow	$\left[\frac{^{\circ}C}{cm}\right]$
κ	thermal diffusivity	$\left[\frac{cm^2}{s}\right]$
ν	kinematic viscosity	$\left[\frac{cm^2}{s}\right]$

*"cm^3 bulk" is cm^3 solid + cm^3 pore space; same for "cm^2 bulk."

where **D** is the hydrodynamic dispersion tensor. The simplification introduced by equations (A8) and (A9) is that they conceal the specific individual factors that control mass transport processes.

The inversions are based on conservation equations that explicitly link bulk fluid transport to mass and tracer changes recorded by the solid. These equations make use of the definitions presented in equations (A8) - (A9) and result from substituting equation (A6) into equation (A1) and equation (A7) into equation (A3),

$$\frac{\partial}{\partial t}(\rho_f\phi) = -\nabla\cdot\mathbf{u} - \frac{D_s}{Dt}[\rho_s(1-\phi)] - \rho_s(1-\phi)\nabla\cdot\mathbf{V}, \tag{A10}$$

$$\frac{\partial}{\partial t}(c_{i,f}\rho_f\phi) = -\nabla\cdot\mathbf{J}_{i,d} - \nabla\cdot\mathbf{J}_{i,a} - \frac{D_s}{Dt}[c_{i,s}\rho_s(1-\phi)] - c_{i,s}\rho_s(1-\phi)\nabla\cdot\mathbf{V} \tag{A11}$$

The absence of source terms (that is, r_f and $r_{i,f}$) in these two equations reflects mass and tracer species conservation between the rock and pore fluid. Because rocks preserve only a cumulative record of fluid-rock interaction, equations (A10) and (A11) need to be integrated with respect to time before field measurements can be used to constrain bulk fluid transport. The operation is performed symbolically and relies on integration by parts and Leibniz's rule. It builds on similar treatments in Baumgartner and Ferry (1991) and Evans and Bickle (1999).

We consider an infiltration event that starts at time t_1 and lasts until time t_2. The total change of solid mass due to chemical processes is quantified by the integration of the material derivative from t_1 to t_2,

$$\int_{t_1}^{t_2}\frac{D_s}{Dt}[\rho_s(1-\phi)]dt = [\rho_s(1-\phi)|_{t_2} - \rho_s(1-\phi)|_{t_1}]_M \equiv \underset{M}{\Delta}\rho_s(1-\phi) \tag{A12}$$

Likewise, the total change in tracer concentration in the solid is

$$\int_{t_1}^{t_2} \frac{D_s}{Dt}\left[c_{i,s}\rho_s(1-\phi)\right]dt = \left[c_{i,s}\rho_s(1-\phi)\big|_{t_2} - c_{i,s}\rho_s(1-\phi)\big|_{t_1}\right]_M \equiv \underset{M}{\Delta} c_{i,s}\rho_s(1-\phi) \tag{A13}$$

The subscript (M) in equations (A12) and (A13) indicates that integration with respect to time is performed following the material reference frame of the solid. The total, time-integrated fluid flux, $\mathbf{q}$, is:

$$\mathbf{q}\big|_{t_1}^{t_2} \equiv \int_{t_1}^{t_2} \mathbf{u}dt \tag{A14}$$

Because fluid composition may change over the duration of the alteration event, $\Delta c_{i,f}$ is defined at times t_1 and t_2 by

$$\begin{aligned} \Delta c_{i,f}\big|_{t_1} &\equiv c_{i,f}\big|_{t_1} - c_{i,f}^{est}, \\ \Delta c_{i,f}\big|_{t_2} &\equiv c_{i,f}\big|_{t_2} - c_{i,f}^{est} \end{aligned} \tag{A15}$$

The $c_{i,f}^{est}$ term in these definitions is typically calculated from a local equilibrium model at given P-T conditions, but the assumption of equilibrium is not essential to the development presented here. In the treatment we followed, as a simplification, $c_{i,f}^{est}$ depends on position in the fossil fluid flow system but not on time (see Ferry, 1995; Ferry and others, 1998, 2005; Penniston-Dorland and Ferry, 2006, for treatments with variable $c_{i,f}^{est}$ using reaction progress as a proxy for time).

A time-integrated tracer mass balance equation can be derived by integrating equations (A10) and (A11) separately, multiplying the time-integrated version of equation (A10) by $c_{i,f}^{est}$, and combining this with the time-integrated version of equation (A11). The resulting expression is:

$$\begin{aligned} &\mathbf{q}\big|_{t_1}^{t_2}\cdot\nabla c_{i,f}^{est} - \underset{M}{\Delta} c_{i,s}\rho_s(1-\phi) + c_{i,f}^{est}\underset{M}{\Delta}\rho_s(1-\phi) = E_{i,1} + E_{i,2} + E_{i,3} + E_{i,4}, \\ &E_{i,1} = -\int_{t_1}^{t_2} \nabla\cdot\mathbf{J}_{i,d}dt, \\ &E_{i,2} = \Delta c_{i,f}\rho_f\phi\big|_{t_1} - \Delta c_{i,f}\rho_f\phi\big|_{t_2} + \nabla\cdot(\mathbf{q}\Delta c_{i,f})\big|_{t_1} - \nabla\cdot(\mathbf{q}\Delta c_{i,f})\big|_{t_2}, \\ &E_{i,3} = c_{i,f}^{est}\int_{t_1}^{t_2} \rho_s(1-\phi)\nabla\cdot\mathbf{V}dt - \int_{t_1}^{t_2} c_{i,s}\rho_s(1-\phi)\nabla\cdot\mathbf{V}dt, \\ &E_{i,4} = \nabla t_1\cdot(\mathbf{u}\Delta c_{i,f})\big|_{t_1} - \nabla t_2\cdot(\mathbf{u}\Delta c_{i,f})\big|_{t_2} + \nabla\cdot\int_{t_1}^{t_2} \mathbf{q}\frac{\partial c_{i,f}}{\partial t}dt \end{aligned} \tag{A16}$$

Equation (A16) is a point-wise balance that relates the total change in tracer concentration in a rock to the cumulative alteration processes affecting the fluid-rock system. The total advective tracer transport through the rock is described by the first term in equation (A16). Advective transport can act as a net supply or sink of a tracer depending on the sign of the vector product in this term. The second term is the difference between the amount of tracer in the rock at the end of the alteration event and at the start of the alteration event. This difference is the basic field observation that is to be interpreted. The third term represents an estimate of tracer changes due to the loss or gain of solid mass. A perfect balance among these three terms is the basis for traditional one-dimensional estimates of time-integrated fluid flux (Baumgartner and Ferry, 1991). The validity of this assumption depends on the remaining terms in equation (A16), which represent additional processes and residuals from the time integration procedure.

The term, $E_{i,1}$, represents the integrated effects of hydrodynamic dispersion during alteration. A dispersive flux with a net negative divergence adds tracer to the rock and a net positive divergent tracer flux removes it from the rock.

The effects of varying fluid compositions during mineral reaction on the time-integrated tracer budget are incorporated in the term, $E_{i,2}$. The first two parts of this term are both likely to be negligible because of the small porosity of metamorphic rocks. The third and fourth parts of $E_{i,2}$ express deviations, $\Delta c_{i,f}$, from the single estimated value of fluid composition, $c_{i,f}^{est}$, at each location. They include any changes in fluid composition caused both by changing tracer concentrations in the solid during the time interval from t_1 to t_2, and by variations due to reaction kinetics.

The term, $E_{i,3}$, accounts for apparent tracer concentration changes caused by solid volume changes due to a divergent solid velocity field. Non-divergent components of the solid velocity field are handled through integration of the material derivative.

The term, $E_{i,4}$, results from the time-integration of the divergence of the advective tracer flux, $\mathbf{J}_{i,a}$. The first two parts of this term show that spatial variations in the timing of infiltration will influence the accounting of the time-integrated tracer budget. The third part of $E_{i,4}$ derives from expanding $\mathbf{J}_{i,a}$ into its separate components before time integration.

We use a compact version of equation (A16), equation (1) in the text, as our model for estimating the time-integrated fluid flux field that drives chemical alteration in a rock. Equation (A17) defines the relationships among the terms in equation (A16) and those in equation (1):

$$\underbrace{\mathbf{q}|_{t_1}^{t_2} \cdot \nabla c_{i,f}^{est}}_{\mathbf{q} \cdot \nabla C_i} - \underbrace{\frac{\Delta c_{i,s} \rho_s (1-\phi)}{M}}_{N_i} + \underbrace{\frac{c_{i,f}^{est} \Delta \rho_s (1-\phi)}{M}}_{C_i N_f} = \underbrace{E_{i,1} + E_{i,2} + E_{i,3} + E_{i,4}}_{e_i} . \qquad \text{(A17)}$$

Equation (A17) considers that devolatilization, N_f, and infiltration, $\mathbf{q}$, of a fluid of constant composition are the dominant controls of chemical alteration of a rock, N_i. Equation (A17), however, explicitly and quantitatively recognizes that this is an imperfect representation of the true process of fluid-rock interaction and allows for an imbalance to exist through the misfit term, e_i.

Appendix B

Model of Heat and Mass Transport Used in Demonstration of the Inversion Methods

We modified an analytical solution from Phillips (1991) to include an exponentially varying permeability with depth in the crust. The permeability structure of the model mediated the density variations that drive flow. Permeability varied exponentially in the vertical direction from 10^{-10} cm^2 at the upper surface of the model to $\approx 10^{-12}$ cm^2 at the base of the model with an e-folding length scale of 1 km, broadly consistent with global compilations of permeability in basaltic oceanic crust (Fisher, 1998).

The solution is governed by a scale ratio, S, that incorporates the geometry and permeability of the model and a Rayleigh number, Ra, that expresses the influence of advective flow on the model's thermal structure (Phillips, 1991):

$$S = \frac{\bar{k}_x}{\bar{k}_z} \left(\frac{D}{L} \right)^2 ;$$

$$Ra = \frac{\bar{k}_x \alpha g D^2}{\kappa \nu} \frac{\partial T}{\partial z} ,$$

where $\bar{k}_x$ is a representative permeability in the x direction, $\bar{k}_z$ is a representative permeability in the z direction, D is a vertical scale of material variation, L is a characteristic horizontal length over which D varies, α is a normalized thermal expansivity, g is gravitational acceleration, κ is thermal diffusivity, ν is kinematic viscosity, and $\partial T/\partial z$ is a representative geothermal gradient. We analytically solved the equations describing fluid continuity, energy conservation, and Darcy's law after accounting for the aspect ratio of the region, a moderate difference in horizontal and vertical permeability, and conductively-controlled heat transport (that is, we adjusted the length and depth of the model domain to scale the general governing equations according to $D/L << 1$, $S << 1$, and $Ra << (L/D)^2$ before solving them). Boundary conditions were an imposed Gaussian distribution of heat flux and no fluid flow at the base of the model domain and constant temperature and fluid pressure at the top. The sides of the model were open to heat and fluid flow. We calculated the oxygen isotopic alteration of a porous rock with an initially homogenous isotopic composition following Dipple and Ferry (1992).

Constant numerical values of dynamical parameters specific to our solution are $\alpha = 3 \times 10^{-4}$ /°C, $\kappa = 10^{-2}$ cm^2/s, and $\nu = 3 \times 10^{-3}$ cm^2/s. The thermal gradient at the base of the model domain varied from 100°C/km at the center of the model to 50°C/km at the margins (fig. 1). The variation was Gaussian in form with a half-width of 40 km. Gradients are within the range predicted by heat flow measurements in oceanic crust older than ≈70 My (Stein and Stein, 1994). At the top of the model, temperature was held at 50°C (fig. 1A), consistent with conductively-cooled abyssal oceanic crust covered by more than 150 m of sediments (Wheat and Mottl, 1994).

The isotopic composition of the infiltrating fluid was held at $\delta^{18}O = 0‰$ where it entered across the upper model boundary, and oxygen isotopes were partitioned between the model fluid and rock given the

results of basalt-water fractionation experiments (Cole and others, 1987), the temperature distribution in figure 1A, and an initial rock $\delta^{18}O = 5.5‰$ (average N-MORB glass; Eiler, 2001). Model rock contains 0.086 mol O/cm^3 rock (Laverne and others, 2001).

References

Abart, R., and Pozzorini, D., 2000, Implications of kinetically controlled mineral-fluid exchange on the geometry of stable-isotope fronts: European Journal of Mineralogy, v. 12, p. 1069–1082.

Abart, R., and Sperb, R., 1997, Grain-scale stable isotope disequilibrium during fluid-rock interaction. 1: Series approximations for advective-dispersive transport and first-order kinetic mineral-fluid exchange: American Journal of Science, v. 297, p. 679–706.

Ague, J. J., 1994, Mass transfer during Barrovian metamorphism of pelites, south-central Connecticut I, Evidence for changes in composition and volume: American Journal of Science, v. 294, p. 989–1057.

——— 1998, Simple models of coupled fluid infiltration and redox reactions in the crust: Contributions to Mineralogy and Petrology, v. 132, p. 180–197.

——— 2003, Fluid infiltration and transport of major, minor, and trace elements during regional metamorphism of carbonate rocks, Wepawaug Schist, Connecticut, USA: American Journal of Science, v. 303, p. 753–816.

——— 2004, Fluid flow in the deep crust, *in* Rudnick, R., editor, The crust: Treatise on Geochemistry, v. 3: Oxford, Elsevier-Pergamon, p. 195–228.

Ague, J. J., and Rye, D. M., 1999, Simple models of CO_2 release from metacarbonates with implications for interpretation of directions and magnitudes of fluid flow in the deep crust: Journal of Petrology, v. 40, p. 1443–1462.

Ague, J. J., and van Haren, J. L. M., 1996, Assessing metasomatic mass and volume changes using the bootstrap, with application to deep crustal hydrothermal alteration of marble: Economic Geology, v. 91, p. 1169–1182.

Albarede, F., 1995, Introduction to geochemical modeling: Cambridge, Cambridge University Press, 543 p.

Allegre, C. J., and Lewin, E., 1989, Chemical structure and history of Earth: Evidence from global non-linear inversion of isotopic data in a three-box model: Earth and Planetary Science Letters, v. 96, p. 61–88.

Backus, G., and Gilbert, F., 1970, Uniqueness in inversion of inaccurate gross earth data: Philosophical Transactions of the Royal Society of London Series A, v. 266, p. 123–292.

Badertscher, N. P., Abart, R., Burkhard., M., and McCaig, A., 2002, Fluid flow pathways along the Glarus overthrust derived from stable- and Sr-isotope patterns: American Journal of Science, v. 302, p. 517–547.

Baker J., and Spiegelman, M., 1995, Modelling an infiltration-driven geochemical front: Earth and Planetary Science Letters, v. 136, p. 87–96.

Baker, T. J., 1999, Delaunay-Voronoï methods, *in* Thompson, J. F., Soni, B. K., and Weatherill, N. P., editors, Handbook of grid generation: Boca Raton, CRC Press, p. 16–1–16–11.

Barnes, H. L., editor, 1997, Geochemistry of hydrothermal ore deposits: New York, John Wiley and Sons, 972 p.

Barnett, D. E., and Chamberlain, C. P., 1991, Relative scales of thermal- and fluid infiltration-driven metamorphism in fold nappes, New England, USA: American Mineralogist, v. 76, p. 713–727.

Baumgartner, L. P., and Ferry, J. M., 1991, A model for coupled fluid flow and mixed-volatile mineral reactions with applications to regional metamorphism: Contributions to Mineralogy and Petrology, v. 106, p. 273–285.

Baumgartner, L. P., and Olsen, S. N., 1995, A least-squares approach to mass-transport calculations using the isocon method: Economic Geology, v. 90, p. 1261–1270.

Baxter, E. F., Ague, J. J., and DePaolo, D. J., 2002, Prograde temperature-time evolution in the Barrovian type-locality constrained by Sm/Nd garnet ages from Glen Clova, Scotland: Journal of the Geological Society, v. 159, p. 71–82.

Berman, R. G., 1988, Internally-consistent thermodynamic data for minerals in the system Na_2O-K_2O-CaO-MgO-FeO-Fe_2O_3-Al_2O_3-SiO_2-TiO_2-H_2O-CO_2: Journal of Petrology, v. 29, p. 455–522.

Bevington, P. R., and Robinson, D. K., 1992, Data reduction and error analysis for the physical sciences: Boston, WCB/McGraw Hill, 328 p.

Bickle, M. J., and Baker, J., 1990, Advective diffusive transport of isotopic fronts: An example from Naxos, Greece: Earth and Planetary Science Letters, v. 97, p. 78–93.

Bickle, M. J., and McKenzie, D., 1987, The transport of heat and matter by fluids during metamorphism: Contributions to Mineralogy and Petrology, v. 95, p. 384–392.

Bickle, M. J., Chapman, H. J., Ferry, J. M., Rumble, D., and Fallick, A. E., 1997, Fluid flow and diffusion in the Waterville limestone, south-central Maine: Constraints from strontium, oxygen and carbon isotope profiles: Journal of Petrology, v. 38, p. 1489–1512.

Blattner, P., and Lassey, K. R., 1989, Stable-isotope exchange fronts, Damköhler numbers, and fluid to rock ratios: Chemical Geology, v. 78, p. 381–392.

Bloxham, J., and Jackson, A., 1992, Time-dependent mapping of the magnetic-field at the core-mantle boundary: Journal of Geophysical Research, v. 97, p. 19537–19563.

Bolin, B., and Keeling, C. D., 1963, Large-scale atmospheric mixing as deduced from seasonal and meridional variations of carbon dioxide: Journal of Geophysical Research, v. 68, p. 3899–3920.

Braun, J., and Sambridge, M., 1995, A numerical-method for solving partial-differential equations on highly irregular evolving grids: Nature, v. 376, p. 655–660.

Breeding, C. M., and Ague, J. J., 2002, Slab-derived fluids and quartz-vein formation in an accretionary prism, Otago Schist, New Zealand: Geology, v. 30, p. 499–502.

Brimhall, G. H., 1979, Lithologic determination of mass-transfer mechanisms of multiple-stage porphyry copper mineralization at Butte, Montana: Vein formation by hypogene leaching and enrichment of potassium-silicate protore: Economic Geology, v. 74, p. 556–589.
Brown, M., 1995, The singular value decomposition method applied to the deduction of the emissions and the isotopic composition of atmospheric methane: Journal of Geophysical Research, v. 100, p. 11425–11446.
Carlson, W. D., 1991, Competitive diffusion-controlled growth of porphyroblasts: Mineralogical Magazine, v. 55, p. 317–330.
Chacko, T., Mayeda, T. K., Clayton, R. N., and Goldsmith, J. R., 1991, Oxygen and carbon isotope fractionations between CO_2 and calcite: Geochimica et Cosmochimica Acta, v. 55, p. 2867–2882.
Chiba, H., Chacko, T., Clayton, R. N., and Goldsmith, J. R., 1989, Oxygen isotope fractionations involving diopside, forsterite, magnetite, and calcite: Application to geothermometry: Geochimica et Cosmochimica Acta, v. 53, p. 2985–2995.
Cole, D. R., and Ripley, E. M., 1999, Oxygen isotope fractionation between chlorite and water from 170 to 350°C: A preliminary assessment based on partial exchange and fluid rock experiments: Geochimica et Cosmochimica Acta, v. 63, p. 449–457.
Cole, D. R., Mottl, M. J., and Ohmoto H., 1987, Isotopic exchange in mineral-fluid systems: II. Oxygen and hydrogen isotopic investigation of the experimental basalt-seawater system: Geochimica et Cosmochimica Acta, v. 51, p. 1523–1538.
Connolly, J. A. D., 1997, Devolatilization-generated fluid pressure and deformation-propagated fluid flow during prograde regional metamorphism: Journal of Geophysical Research, v. 102, p. 18149–18173.
Constable, S. C., Parker, R. L., and Constable, C. G., 1987, Occam's inversion: A practical algorithm for generating smooth models from electromagnetic sounding data: Geophysics, v. 52, p. 289–300.
Cui, X. J., Nabelek, P. I., and Liu, M. A., 2003, Reactive flow of mixed CO_2-H_2O fluid and progress of calc-silicate reactions in contact metamorphic aureoles: Insights from two-dimensional numerical modeling: Journal of Metamorphic Geology, v. 21, p. 663–684.
Dipple, G. M., and Ferry, J. M., 1992, Fluid flow and stable isotopic alteration in rocks at elevated temperatures with applications to metamorphism: Geochimica et Cosmochimica Acta, v. 56, p. 3539–3550.
Doll, C. G., Cady, W. M., Thompson, J. B., Jr., and Billings, M. B., 1961, Centennial geologic map of Vermont: Vermont Geological Survey, scale 1:250,000.
Efron, B., and Tibrshirani, R. J., 1993, An introduction to the bootstrap: New York, Chapman and Hall, 436 p.
Eiler, J. M., 2001, Oxygen isotope variations of basaltic lavas and upper mantle rocks, *in* Valley, J. W., and Cole, D. R., editors, Stable isotope geochemistry: Mineralogical Society of America, Reviews in Mineralogy and Geochemistry, v. 43, p. 319–364.
Eppel, H., and Abart, R., 1997, Grain-scale stable isotope disequilibrium during fluid-rock interaction. 2: An example from the Penninic-Austroalpine tectonic contact in eastern Switzerland: American Journal of Science, v. 297, p. 707–728.
Evans, K. A., and Bickle, M. J., 1999, Determination of time-integrated metamorphic fluid fluxes from the reaction progress of multivariant assemblages: Contributions to Mineralogy and Petrology, v. 134, p. 277–293.
Ferry, J. M., 1988, Infiltration-driven metamorphism in northern New England, USA: Journal of Petrology, v. 29, p. 1121–1159.
——— 1992, Regional metamorphism of the Waits River Formation, eastern Vermont: Delineation of a new type of giant metamorphic hydrothermal system: Journal of Petrology, v. 33, p. 45–94.
——— 1994, Overview of the petrologic record of fluid flow during regional metamorphism in northern New England: American Journal of Science, v. 294, p. 905–988.
——— 1995, Fluid flow during contact metamorphism of ophicarbonate rocks in the Bergell aureole, Val Malenco, Italian Alps: Journal of Petrology, v. 36, p. 1039–1053.
Ferry, J. M., Sorensen, S. S., and Rumble, D., III, 1998, Structurally controlled fluid flow during contact metamorphism in the Ritter Range pendant, California, USA: Contributions to Mineralogy and Petrology, v. 130, p. 358–378.
Ferry, J. M., Rumble, D., III, Wing, B. A., and Penniston-Dorland, S. C., 2005, A new interpretation of centimetre-scale variations in the progress of infiltration-driven metamorphic reactions: Case study of carbonated metaperidotite, Val d'Efra, Central Alps, Switzerland: Journal of Petrology, v. 46, p. 1725–1746.
Fiadeiro, M. E., and Veronis, G., 1984, Obtaining velocities from tracer distributions: Journal of Physical Oceanography, v. 14, p. 1734–1746.
Finlayson, B. A., 1972, The method of weighted residuals and variational principles: New York, Academic Press, 412 p.
Fisher, A. T., 1998, Permeability within basaltic oceanic crust: Reviews of Geophysics, v. 36, p. 143–182.
Fisher, A. T., and Becker, K., 2000, Channelized fluid flow in oceanic crust reconciles heat-flow and permeability data: Nature, v. 403, p. 71–74.
Gaillardet, J., Dupré, B., Louvat, P., and Allegre, C. J., 1999, Global silicate weathering and CO_2 consumption rates deduced from the chemistry of large rivers: Chemical Geology, v. 159, p. 3–30.
Gerdes, M. L., Baumgartner, L. P., Person, M., and Rumble, D., III, 1995, One- and 2-dimensional models of fluid flow and stable-isotope exchange at an outcrop in the Adamello contact aureole, Southern Alps, Italy: American Mineralogist, v. 80, p. 1004–1019.
Gubbins, D., 1982, Finding core motions from magnetic observations: Philosophical Transactions of the Royal Society of London Series A, v. 306, p. 247–254.

Hanson, R. B., 1992, Effects of fluid production on fluid flow during regional and contact metamorphism: Journal of Metamorphic Geology, v. 10, p. 87–97.
——— 1995, Hydrodynamics of contact metamorphism: Geological Society of America Bulletin, v. 107, p. 595–611.
——— 1997, Hydrodynamics of regional metamorphism due to continental collision: Economic Geology, v. 92, p. 880–891.
Hatch, N. L., Jr., 1988, Some revisions to the structure and stratigraphy of the Connecticut Valley trough, eastern Vermont: American Journal of Science, v. 288, p. 1041–1059.
Hepburn, C. J., Trask, N. J., Rosenfeld, J. L., and Thompson, J. B., Jr., 1984, Bedrock geology of the Brattleboro quadrangle, Vermont-New Hampshire: Vermont Geological Survey Bulletin 32, 162 p.
Hueber, F. M., Bothner, W. A., Hatch, N. L., Jr., Finney, S. C., and Aleinikoff, J. N., 1990, Devonian plants from southern Quebec and northern New Hampshire and the age of the Connecticut Valley trough: American Journal of Science, v. 290, p. 360–395.
Kerrick, D. M., 2001, Present and past nonanthropogenic CO_2 degassing from the solid Earth: Reviews of Geophysics, v. 39, p. 565–585.
Kerrick, D. M., and Caldeira, K., 1998, Metamorphic CO_2 degassing from orogenic belts: Chemical Geology, v. 145, p. 213–232.
Kohn, M. J., and Valley, J. W., 1994, Oxygen-isotope constraints on metamorphic fluid flow, Townshend Dam, Vermont, USA: Geochimica et Cosmochimica Acta, v. 58, p. 5551–5566.
Laverne, C., Agrinier, P., Hermitte, D., and Bohn, M., 2001, Chemical fluxes during hydrothermal alteration of a 1200m long section of dikes in the oceanic crust, DSDP/ODP Hole 504B: Chemical Geology, v. 181, p. 73–98.
Léger, A., and Ferry, J. M., 1993, Fluid infiltration and regional metamorphism of the Waits River Formation, north-east Vermont, USA: Journal of Metamorphic Geology, v. 11, p. 3–29.
Lichtner, P. C., 1996, Continuum formulation of multicomponent-multiphase reactive transport, *in* Lichtner, P. C., Steefel, C. I., and Oelkers, E. H., editors, Reactive transport in porous media: Mineralogical Society of America, Reviews in Mineralogy, v. 34, p. 1–81.
Manning, C. E., and Ingebritsen, S. E., 1999, Permeability of the continental crust: Implications of geothermal data and metamorphic systems: Reviews of Geophysics, v. 37, p. 127–150.
Matsuhisa, Y., Goldsmith, J. R., and Clayton, R. N., 1979, Oxygen isotopic fractionation in the system quartz-albite-anorthite-water: Geochimica et Cosmochimica Acta, v. 43, p. 1131–1140.
Matthews, A., Goldsmith, J. R., and Clayton, R. N., 1983, Oxygen isotope fractionation between zoisite and water: Geochimica et Cosmochimica Acta, v. 47, p. 645–654.
McKenzie, D., and O'Nions, R. K., 1991, Partial melt distributions from inversion of rare earth element concentrations: Journal of Petrology, v. 32, p. 1021–1091.
Menard, T., and Spear, F. S., 1994, Metamorphic P-T paths from calcic pelitic schists from the Strafford Dome, Vermont, USA: Journal of Metamorphic Geology, v. 12, p. 811–826.
Menke, W., 1989, Geophysical data analysis: Discrete inverse theory: Orlando, Academic Press, 260 p.
Osberg, P. H., Tull, J. F., Robinson, P., Hon., R., and Butler, J .B., 1989, The Acadian orogen, *in* Hatcher, R. D., Jr., Thomas, W. A., and Viele, G. W., editors, The Appalachian-Ouchita orogen in the United States, The Geological Society of America, v. F-2, Boulder: Geological Society of America, Geology of North America, p. 179–232.
Parker, R. L., 1977, Understanding inverse theory: Annual Review of Earth and Planetary Sciences, v. 5, p. 35–64.
——— 1994, Geophysical inverse theory: Princeton, Princeton University Press, 386 p.
Penniston-Dorland, S. C., and Ferry, J. M., 2006, Development of spatial variations in reaction progress during regional metamorphism of micaceous carbonate rocks, northern New England: American Journal of Science, v. 306, p. 475–524.
Phillips, O. M., 1991, Flow and reactions in permeable rocks: Cambridge, Cambridge University Press, 285 p.
Provost, C., and Salmon, R., 1986, A variational method for inverting hydrographic data: Journal of Marine Research, v. 44, p. 1–34.
Rau, S., Christensen, U., Jackson, A., and Wicht, J., 2000, Core flow inversion tested with numerical dynamo models: Geophysical Journal International, v. 141, p. 485–497.
Rice, J. M., and Ferry, J. M., 1982, Buffering, infiltration, and the control of reaction progress during metamorphic devolatilization reactions, *in* Ferry, J. M., editor, Characterization of metamorphism through mineral equilibria: Mineralogical Society of America, Reviews in Mineralogy, v. 10, p. 263–326.
Rosenfeld, J. L., 1968, Garnet rotations due to the major Paleozoic deformations in southeast Vermont, *in* Zen, E-an, White, W. S., Hadley, J. B., and Thompson, J. B., Jr., editors, Studies in Appalachian geology: Northern and Maritime: New York, Interscience, p. 185–202.
Rumble, D., III, 1982, Stable isotope fractionation during metamorphic devolatilization reactions, *in* Ferry, J. M., editor, Characterization of metamorphism through mineral equilibria: Mineralogical Society of America, Reviews in Mineralogy, v. 10, p. 327–353.
Shaw, D. M., 1956, Geochemistry of pelitic rocks. Part III: Major elements and general geochemistry: Geological Society of America Bulletin, v. 67, p. 919–934.
Sheppard, S. M. F., and Schwarcz, H. P., 1970, Fractionation of carbon and oxygen isotopes and magnesium between coexisting metamorphic calcite and dolomite: Contributions to Mineralogy and Petrology, v. 26, p. 161–98.
Skelton, A. D. L., Graham, C. M., and Bickle, M. J., 1995, Lithological and structural controls on regional 3-D fluid-flow patterns during greenschist facies metamorphism of the Dalradian of the SW Scottish Highlands: Journal of Petrology, v. 36, p. 563–586.
Spear, F. S., Kohn, M. J., Cheney, J. T., and Florence, F., 2002, Metamorphic, thermal, and tectonic evolution of central New England: Journal of Petrology, v. 43, p. 2097–2120.

Spiegelman, M., Kelemen, P. B., and Aharonov, E., 2001, Causes and consequences of flow organization during melt transport: The reaction infiltration instability in compactable media: Journal of Geophysical Research, v. 106, p. 2061–2077.
Stein, C. A., and Stein, S., 1994, Constraints on hydrothermal heat flux through the oceanic lithosphere from global heat flow: Journal of Geophysical Research, v. 99, p. 3081–3095.
Stern, L. A., Chamberlain, C. P., Barnett, D. E., and Ferry, J. M., 1992, Stable-isotopic evidence for regional-scale fluid migration in a Barrovian metamorphic terrane, Vermont, USA: Contributions to Mineralogy and Petrology, v. 112, p. 475–489.
Taylor, H. P., Jr., 1977, Water/rock interactions and the origin of H_2O in granitic batholiths: London, Journal of the Geological Society, v. 133, p. 509–558.
Thompson, J. B., Jr., and Norton, S. A., 1968, Paleozoic regional metamorphism in New England and adjacent areas, *in* Zen, E-an, White, W. S., Hadley, J. B., and Thompson, J. B., Jr., editors, Studies in Appalachian geology: Northern and Maritime: New York, Interscience, p. 319–327.
Thompson, J. B., Jr., Robinson, P., Clifford, T. N., and Trask, N. J., 1968, Nappes and gneiss domes in west-central New England, *in* Zen, E-an, White, W. S., Hadley, J. B., and Thompson, J. B., Jr., editors, Studies in Appalachian geology: Northern and Maritime: New York, Interscience, p. 203–218.
Tilmann, F., Ni, J., and INDEPTH III Seismic Team, 2003, Seismic imaging of the downwelling Indian lithosphere beneath central Tibet: Science, v. 300, p. 1424–1427.
van Haren, J. L. M., Ague, J. J., and Rye, D. M., 1996, Oxygen isotope record of fluid infiltration and mass transfer during regional metamorphism of pelitic schist, Connecticut, USA: Geochimica et Cosmochimica Acta, v. 60, p. 3487–3504.
van Wijk, K., Scales, J. A., Navidi, W., and Tenorio, L., 2002, Data and model uncertainty estimation for linear inversion: Geophysical Journal International, v. 149, p. 625–632.
Vyhnal, C. R., and Chamberlain, C. P., 1996, Preservation of early isotopic signatures during prograde metamorphism, eastern Vermont: American Journal of Science, v. 296, p. 394–419.
Walther, J. V., and Orville, P. M., 1982, Volatile production and transport in regional metamorphism: Contributions to Mineralogy and Petrology, v. 79, p. 252–257.
Watson, D. F., 1992, Contouring: A guide to the analysis and display of spatial data: Oxford, Pergamon, 321 p.
West, M., Menke, W., Tolstoy, M., Webb, S., and Sohn, R., 2001, Magma storage beneath axial volcano on the Juan de Fuca mid-ocean ridge: Nature, v. 413, p. 833–836.
Wheat, C. G., and Mottl, M. J., 1994, Hydrothermal circulation, Juan de Fuca ridge eastern flank: Factors controlling basement water composition: Journal of Geophysical Research, v. 99, p. 3067–3080.
Wing, B. A., and Ferry, J. M., 2002, Three-dimensional geometry of metamorphic fluid flow during Barrovian regional metamorphism from an inversion of combined petrologic and stable isotopic data: Geology, v. 30, p. 639–642.
Wing, B. A., Ferry, J. M., and Harrison, T. M., 2003, Prograde destruction and formation of monazite and allanite during contact and regional metamorphism of pelites: Petrology and geochronology: Contributions to Mineralogy and Petrology, v. 145, p. 228–250.
Wunsch, C., 1978, North Atlantic general circulation west of 50°W determined by inverse methods: Reviews of Geophysics, v. 16, p. 583–620.
——— 1996, The ocean circulation inverse problem: Cambridge, United Kingdom, Cambridge University Press, 442 p.
Zheng, Y. F., Metz, P., and Satir, M., 1994, Oxygen-isotope fractionation between calcite and tremolite: An experimental study: Contributions to Mineralogy and Petrology, v. 118, p. 249–255.
Zienkiewicz, O. C., and Morgan, K., 1983, Finite elements and approximation: New York, John Wiley and Sons, 328 p.